Atmos. Chem. Phys. Discuss., 14, 28385–28452, 2014
www.atmos-chem-phys-discuss.net/14/28385/2014/
doi:10.5194/acpd-14-28385-2014

Atmospheric Chemistry and Physics Discussions

Constraining black carbon aerosol over Southeast Asia using OMI aerosol absorption optical depth and the adjoint of GEOS-Chem

L. Zhang[1,2], D. K. Henze[1], G. A. Grell[2], G. R. Carmichael[3], N. Bousserez[1], Q. Zhang[4], and J. Cao[5]

[1]Department of Mechanical Engineering, University of Colorado, 1111 Engineering Drive ECES 114, Boulder, CO, USA
[2]Global Systems Division, Earth System Research Laboratory, NOAA, Boulder, CO, USA
[3]Department of Chemical and Biochemical Engineering, University of Iowa, Iowa, IA, USA
[4]Center for Earth System Science, Tsinghua University, Beijing, China
[5]Key Lab of Aerosol Chemistry & Physics, Institute of Earth Environment, Chinese Academy of Sciences, Xi'an, China

Received: 19 August 2014 – Accepted: 22 October 2014 – Published: 17 November 2014

Correspondence to: D. K. Henze (daven.henze@colorado.edu)

Published by Copernicus Publications on behalf of the European Geosciences Union.

Abstract

Accurate estimates of the emissions and distribution of Southeast Asian (70–150° E, 11° S–55° N) black carbon (BC) are critical to studies of the atmospheric environment and climate change. Analysis of modeled BC concentrations compared to in situ observations indicates levels are underestimated over most of Southeast Asia when using any of four different emission inventories. We thus attempt to reduce uncertainties in BC emissions and improve BC model simulations by developing top-down, spatially resolved, estimates of BC emissions through assimilation of OMI observations of aerosol absorption optical depth (AAOD) with the GEOS-Chem model and its adjoint for April and October of 2006. Overwhelming enhancements, up to 500 %, in anthropogenic BC emissions are shown after optimization over broad areas of Southeast Asia in April. In October, the optimization of anthropogenic emissions yields a slight reduction (1 ∼ 5 %) over India and parts of southern China, while emissions increase by 10 ∼ 50 % over eastern China. Observational data from in situ measurements and AERONET observations are used to evaluate the BC inversions and assess the bias between OMI and AERONET AAOD. Low biases in BC concentrations are improved or corrected in most eastern and central sites over China after optimization, while the constrained model still underestimates concentrations in Indian sites in both April and October, possibly as a consequence of low prior emissions. Model resolution errors may contribute up to a factor of 2.5 to the underestimate of surface BC concentrations over northern India. We also compare the optimized results using different anthropogenic emission inventories and discuss the sensitivity of top-down constraints on anthropogenic emissions with respect to biomass burning emissions. In addition, the impacts of different observation operators and a priori constraints on the optimization are investigated. Overall, despite these limitations and uncertainties, using OMI AAOD to constrain BC sources improves model representation of BC distributions, particularly over China.

ACPD
14, 28385–28452, 2014

1 Introduction

Black carbon (BC) is a product of incomplete combustion of carbonaceous fuels, enhanced concentrations of which have led to a present-day overall positive radiative forcing and climate warming (Bond et al., 2013). More than ten years ago, Jacobson (2000) and Hansen et al. (2000) recognized that preindustrial to present increases in BC might warm the atmosphere about one third as much as CO_2. Recently, an assessment report by Bond et al. (2013) indicates that the global average preindustrial to present radiative forcing from BC is +1.1 W m^{-2} with 90 % uncertainty bounds of +0.17 to +2.1 W m^{-2}, which is more than two thirds that of CO_2 (+1.56 W m^{-2}). Additionally, BC aerosols constitute up to 10–15 % of the mass concentration of fine particulate matter ($PM_{2.5}$) over continental regions, exposure to which is known to adversely effect human health (e.g., Janssen et al., 2005, 2011; Schwartz et al., 2008; Li et al., 2014). Given the magnitude of BC climate effects and health impacts, a number of studies have investigated its direct effect (Forster, 2007; Ramanathan and Carmichael, 2008), semi-direct effect (Ackeman et al., 2000; Johnson et al., 2004), indirect effect (Cozic et al., 2007; Liu et al., 2009; Oshima et al., 2009), and the albedo effect when deposited on snow (Hansen and Nazarenko, 2004; Hansen et al., 2005; Flanner et al., 2007; Qian et al., 2009) using various numerical models and observations.

Central estimates of global annual emissions of BC are 8.0 Tg, of which 38 % comes from fossil fuel, 20 % from biofuel and 42 % from open burning (Bond et al., 2004). At the same time, estimates of BC emissions are recognized as having large uncertainties – (50 %) at global scales and a factor of two to five at regional scales (Bond et al., 2004; Ramanathan and Carmichael, 2008). Southeast Asia (70–150° E, 11° S–55° N) is the major anthropogenic BC source region in the world, with growth in BC emissions of 21 % over China and 41 % over India from 1996 to 2010 associated with rapid economic and industrial development (Lu et al., 2011). BC emissions from both energy-related combustion and biomass burning that occur largely in Asia and Africa currently appear underestimated (Bond et al., 2013). A global top-down estimate of BC

ACPD
14, 28385–28452, 2014

emission using AERONET observation by Cohen and Wang (2014) indicated that commonly used global BC emissions datasets may be underestimated by a factor of two or more. Sixteen models from the AeroCom aerosol model intercomparisons underestimated the Southeast Asian BC surface concentrations by a factor of 2 ∼ 3 (Koch et al., 2009). The GEOS-Chem model also underestimated monthly BC concentrations at almost all rural sites in China, particularly in January 2006, which indicated a regional underprediction of carbonaceous aerosol sources associated with anthropogenic activities (Fu et al., 2012; Wang et al., 2013). In addition, the global atmospheric absorption attributable to BC is too low in many global aerosol models by a factor of almost three on a global mean basis, which can be attributed to the models lacking treatment of enhanced absorption caused by mixing of BC with other constituents and the amount of BC in the atmosphere (Bond et al., 2013). On the other hand, a typical fresh particle mass absorption cross section (MABS, essentially the column BC absorption divided by the load) of about 7.5 $m^2 g^{-1}$ recommended by Bond and Bergstrom (2006) is not represented in most models, which should probably increase as particles age (Koch et al., 2009). This bias would also impact simulated AAOD, and inferences about emissions based on such comparisons would likewise be biased.

To reduce uncertainties in BC emissions and improve poor representation of BC in model simulations, different top-down approaches have been used to constrain bottom up BC emissions, such as the linear constraints between concentrations and emissions (Park et al., 2003; Kondo et al., 2011; Fu et al., 2012; Wang et al., 2013), inverse modeling using the decoupled direct method (Hu et al., 2009a, b), the Kalman filter technique (Cohen and Wang, 2014), and the adjoint based 4-D variational approach (Hakami et al., 2005). These studies have exclusively used in situ measurements or airborne observations, which can provide accurate observations of aerosol properties. However, they are often incomplete in their spatial or temporal coverage. Satellite measurements of aerosol optical depth (AOD) have much broader temporal and spatial coverage, and have also been used to constrain BC sources (Huneeus et al., 2003; Xu et al., 2013). However, AOD reflects the contribution from all aerosol components,

ACPD
14, 28385–28452, 2014

making it difficult to distinguish and quantify different aerosol species, especially their relative fractions.

The OMI aerosol absorption optical depth (AAOD), the non-scattering part of the AOD, is an atmospheric column measurement of absorbing aerosol particles, i.e., absorbing carbon and mineral dust, which provides a different perspective to constrain BC sources (Torres et al., 1998; Koch et al., 2009). In this study, the GEOS-Chem adjoint model and satellite observations of OMI AAOD are used to constrain spatially resolved BC emissions. Our study will focus on April and October to compare times when the dust loading is relatively large and small over Southeast Asia. Section 2 describes the observations, emissions, and forward and inverse model used in this study. Then we quantify discrepancies between observations and model estimates based on different BC anthropogenic emissions in Sect. 3. Section 4 describes how formulation of the inverse problem affects the results; evaluation of the inversion results with different prior emission inventories and independent observations are presented in Sect. 5, and we end with discussion and conclusions in Sect. 6.

2 Data and models

2.1 Observations

2.1.1 OMI AAOD

The Ozone Monitoring Instrument (OMI) aboard Aura is a nadir-viewing, wide-swath hyper-spectral imaging spectrometer that provides daily global coverage with high spectral resolutions and spatial resolution of 13 km × 24 km at nadir (Levelt et al., 2006a). It detects backscattered solar radiance in the ultraviolet-visible wavelengths (0.27 to 0.5 µm) to measure aerosols, clouds, surface UV irradiance, and trace gases (Levelt et al., 2006b). OMI takes advantage of the greater sensitivity of radiances measured at the top-of-atmosphere in the near-UV region to the varying load and type of

ACPD
14, 28385–28452, 2014

aerosols to derive extinction AOD, single scattering albedo (SSA), and AAOD using an inversion procedure at 354, 388 and 500 nm generated by the near-UV (OMAERUV) algorithm (Torres et al., 2007). The optical depths at 388 nm are inverted from radiance observations while the 354 and 500 nm results are obtained by conversion of the 388 nm retrievals. The OMAERUV retrieval algorithm is particularly sensitive to carbonaceous and mineral aerosols. The OMAERUV retrieval algorithm assumes that the column aerosol load can be represented by one of three types of aerosols and uses a set of aerosol models to account for the presence of these aerosols: carbonaceous aerosol from biomass burning, desert dust, and light absorbing sulfate-based aerosols. Each aerosol type is represented by seven aerosol models of varying single scattering albedo, for a total of twenty-one models. The twenty-one aerosol models used by OMAERUV are based on long-term statistics of ground-based observations by the AERONET. Due the large sensitivity of the OMI near UV observations to particle absorption, the AAOD is the most reliable quantitative OMAERUV aerosol parameter, especially over land. The root-mean-square error for AAOD is estimated to be ~ 0.01[1].

Since the retrieval algorithm is sensitive to the aerosol height, the Level 2 OMI AAOD data reports a set of retrieved parameters for different assumptions of the altitude of the aerosol center of mass: at the surface, and at 1.5, 3.0, 6.0 and 10.0 km above the surface (Torres et al., 2005). For carbonaceous and desert dust particles, the aerosol load is assumed to be vertically distributed following a Gaussian function characterized by peak (aerosol layer height) and half-width (aerosol layer geometric thickness) values (Torres et al., 2005, 2013). The retrieval values of AAOD are much larger if using the aerosol layer altitude where more absorbing aerosols are loaded. In general, when comparing satellite retrievals of trace gases with other measurements or model simulations, it is essential to take into account the different sensitivities of the instruments by applying averaging kernels (Luo et al., 2007; Worden et al., 2007). However, there is no averaging kernel for OMI AOD/AAOD retrievals. It is thus important to consider differ-

[1] daac.gsfc.nasa.gov/Aura/data-holdings/OMI/documents/v003/OMAERUV_README_V003.doc

ACPD
14, 28385–28452, 2014

ences in aerosol properties and distributions used in the retrieval algorithm with those in the assimilation model (e.g., GEOS-Chem). The retrieval "Final AAOD" products are interpolated values using the aerosol layer height value given by the CALIPOSO-based climatology (OMI_Final) (Torres et al., 2013). In order to obtain a consistent vertical profile between the OMI retrieval and GEOS-Chem, we use the GEOS-Chem simulated aerosol layer height instead of the CALIOP-based aerosol layer height climatology to calculate a GEOS-Chem-based OMI AAOD (OMI_GC AAOD) as a linear interpolation of the OMI AAOD values corresponding to different assumed peak heights. Figure 1 shows the differences between OMI_Final and OMI_GC AAOD over Southeast Asia for April and October 2006. In April, the enhancements from applying the GEOS-Chem aerosol layer height are quite significant, with 30–50 % increases over eastern China and downwind areas while 20–30 % increases over India and southeastern Asia, since the simulated aerosol layer heights are much lower than those of OMI-based. The increases even exceed 60 % across broad areas over the tropical ocean. Some reductions are shown over parts of western China and northern Asia in the OMI_GC AAOD. In October, the patterns of enhancement and reduction are similar to those in April, with smaller changes (less than 20 %) over broad continental areas. The most significant differences are dominated by the major aerosol source regions, such as eastern China and South Asia.

2.1.2 AERONET AAOD

The Aerosol Robotic Network (AERONET) is a ground-based instrument network providing a long-term, continuous and readily accessible public domain database of aerosol optical, microphysical and radiative properties (Holben et al., 1998). AERONET inversion code provides aerosol optical properties (including size distribution, refractive index, and single scattering albedo) in the total atmospheric column derived from the direct and diffuse radiation measured by Cimel sun/sky-radiometers (Dubovik and King, 2000; Dubovik et al., 2000, 2002a, b, 2006; Sinyuk et al., 2007).

ACPD
14, 28385–28452, 2014

We use Level 2.0 quality-assured AERONET aerosol inversions data of AAOD at 440 nm. The prefield and postfield calibrations have been applied in these measurements and they were cloud cleared and manually inspected (Omar et al., 2013). The total uncertainty in the AERONET AOD for field instruments is ±0.1 to ±0.2 and is spectrally dependent with the higher errors (±0.2) in the UV spectral range (Eck et al., 1999). The retrieved single scattering albedo uncertainties were within 0.03, estimated by Dubovik et al. (2000), with the exception of the 0.44 µm retrievals for the desert dust case when they increased by ∼ 0.09 and 0.07 for low and high aerosol loadings, respectively (Sinyuk et al., 2007).

2.1.3 In situ measurements

For the monthly surface BC observation over Southeast Asia, we combine the in situ measurements of BC concentration based on several published studies (Zhang et al., 2008; Beegum et al., 2009; Moorthy et al., 2013). Over China, the monthly surface BC concentrations are from 12 sites, including urban sites and rural sites for April and October 2006, which were based on results of Zhang et al. (2008). The locations of these 12 sites are shown in Fig. 2. The BC concentrations are analyzed by using thermo-chemical analysis from PM_{10} aerosols, which were collected by air sample (Zhang et al., 2008). The daily BC measurements are only available at the site of Xi'an (XIA). The $PM_{2.5}$ BC concentrations were measured continuously as 5 min averages by quartzfiber filter tape transmission at an 880 nm wavelength with an aethalometer (Hansen et al., 1984). More details about the measurement methods are described by Cao et al. (2007, 2009).

The measurements of monthly surface BC concentrations for 2006 using aethalometers over India were based on Beegum et al. (2009) and Moorthy et al. (2013), which were carried out in eight sites (see Table 1) covering India and adjacent oceanic regions. Locations of these sites are indicated in Fig. 2. More details about the measurements and sites are described by Beegum et al. (2009). DEL and KGP represent urban and semi-urban sites in the Indo-Gangetic Plain (IGP). HYD and PUN represent

ACPD
14, 28385–28452, 2014

urban locations. TVM is a semi-urban coastal station in the south India; NTL is a high altitude location in the central Himalayas, and MCY and PBR are two island locations representing the Arabian Sea and Bay of Bengal, respectively.

2.2 GEOS-Chem

GEOS-Chem is a global three-dimension chemical transport model driven by assimilated meteorological observations from the Goddard Earth Observing System (GEOS) of the NASA Global Modeling and Assimilation Office (GMAO) (Bey et al., 2001). We use the nested-grid GEOS-Chem model (Wang et al., 2004; Chen et al., 2009) driven by GEOS-5 meteorological fields with 6 h temporal resolution (3 h for surface variables and mixing depths), 0.5° (latitude) × 0.667° (longitude) horizontal resolution over the window of Southeast Asia (70–150° E, 11° S–55° N), and 47 vertical layers between the surface and 0.01 hPa. A global simulation with lower resolution of 4° (latitude) × 5° (longitude) provides the lateral boundary conditions to the higher resolution nested-grid simulation every 3 h.

The original carbonaceous aerosol simulation in GEOS–Chem was developed by Park et al. (2003). It assumes that 80 % of BC and 50 % of OC emitted from primary sources are hydrophobic and that hydrophobic aerosols become hydrophilic with an e-folding time of 1.15 days (Park et al., 2003; Chin et al., 2002; Cooke et al., 1999). Dust in GEOS-Chem is distributed across four size bins (radii 0.1–1.0, 1.0–1.8, 1.8–3.0, and 3.0–6.0 µm) following Ginoux et al. (2004). The smallest size bin is further divided equally into four sub-micron size bins (with effective radii centered at 0.15, 0.25, 0.4 and 0.8 µm) for calculation of optical properties and heterogeneous chemistry (Fairlie et al., 2010; Ridley et al., 2012). Due to the significant positive biases identified in GEOS-Chem dust simulations both in surface concentration and dust AOD (Fairlie et al., 2010; Ku and Park, 2011; Ridley et al., 2012; Wang et al., 2012), a new emitted dust particle size distribution (PSD) based upon scale-invariant fragmentation theory (Kok, 2011) with constraints from in situ measurements (Zhao et al., 2010) is implemented in GEOS-Chem to improve the dust simulation (Zhang et al., 2013). Large

ACPD
14, 28385–28452, 2014

discrepancies are reduced between the simulated surface-level fine dust concentration and measurements from the IMPROVE network in the western US during March to May of 2006 (Zhang et al., 2013). The new PSD also improves the positive biases of AOD over the Asian and African dust source region in April 2006 (See Fig. S1 in Supplement). The wet deposition scheme (Liu et al., 2001) includes scavenging in convective updrafts as well as in-cloud and below-cloud scavenging from convective and large-scale precipitation. Dry deposition is based on the resistance-in-series scheme of Wesely (1989) as implemented by Wang et al. (1998).

2.3 BC emission inventories

Emissions of BC from biomass burning sources are taken from version 2 of the GFED 8 day inventory (van der Werf et al., 2006; Randerson et al., 2006). GFED v2 is derived using satellite observations of active fire counts and burned areas in conjunction with the Carnegie–Ames–Stanford-Approach (CASA) biogeochemical model. Carbon emissions are calculated as the product of burned area, fuel load and combustion completeness. Burned area is derived using the active fire and 500-meter burned area datasets from the Moderate Resolution Imaging Spectroradiometer (MODIS) as described by Giglio et al. (2006). We also use a new version of GFED v3 daily emissions for sensitivity analysis (van der Werf et al., 2010). Compared to GFED v2, the main update in GFED v3 is the spatial resolution of the global grid is quadrupled from 1° to 0.5°, the native 500 m MODIS daily burned area maps are applied (Giglio et al., 2010), the regional regression trees of GFEDv2 are replaced by a local regression approach in producing the indirect, active-fire based estimates of burned area, and a revised version of Carnegie–Ames–Stanford-Approach (CASA) biogeochemical model is used.

Global anthropogenic emissions for carbonaceous aerosols (BC/OC) in GEOS-Chem are originally from Bond et al. (2004, 2007), which contain both biofuel and fossil fuel emissions. The estimated BC emissions uncertainties are −36 to 149 % over China and 38 to −119 % for India (Bond et al., 2004; Lu et al., 2011). In this study, we evaluate three additional carbonaceous anthropogenic emission inventories

ACPD
14, 28385–28452, 2014

over the Southeast Asia and China: the Streets regional inventory for Intercontinental Chemical Transport Experiment – Phase B (INTEX-B), the Southeast Asia Composition, Cloud, Climate Coupling Regional Study (SEAC^{4}RS) emission inventory, and the Multi-resolution Emission Inventory for China (MEIC, http://www.meicmodel.org/). Anthropogenic emissions are all classified into four major sectors: power generation, industry, residential and transport. The INTEX-B inventory is based on 2006 and contains monthly variations with 0.5° × 0.5° horizontal resolution over Southeast Asia (Zhang et al., 2009). The SEAC^{4}RS inventory is an annual, finer resolution inventory based on 2012, with 0.1° × 0.1° horizontal resolution over Southeast Asia (Lu et al., 2011). The average uncertainties of BC are estimated to be −43 to 90 % over China, which are much lower than those of the INTEX-B between −68 to 308 % (Zhang et al., 2009; Lu et al., 2011). The MEIC emission inventory over China also includes monthly variations and is provided at the 0.5° × 0.5° horizontal resolution. These four anthropogenic emission inventories are regridded to the GEOS-Chem resolution of 0.5° × 0.667°, and their annual emissions are shown in Fig. 3. The differences in these inventories exceed 100 % across broad areas, especially over India and eastern China. The anthropogenic emission inventory of INTEX-B is comparable to that of MEIC over eastern China while lower than that of Bond and SEAC^{4}RS over western China and India. Both Bond and SEAC^{4}RS inventories are lower over central and eastern China compared to those of INTEX-B and MEIC inventories. With much finer resolution, the SEAC^{4}RS emission inventory indicates more hot spots spread across eastern and central China and the IGP and eastern India where rural population densities are high and residential coal and biofuel combustion are prevalent (Lu et al., 2011).

2.4 GEOS-Chem adjoint and inverse modeling

An adjoint model is a set of equations auxiliary to a forward model that are used to efficiently calculate the gradient of a scalar model response function with respect to all model parameters simultaneously (Lions, 1971). The adjoint of GEOS-Chem was developed specifically for inverse modeling including explicit treatment of gas-phase

ACPD
14, 28385–28452, 2014

chemistry, heterogeneous chemistry, black and organic primary aerosol, as well as the treatment of the thermodynamic couplings of the sulfate-ammonium-nitrate-formation chemistry (Henze et al., 2007, 2009), with code updates following the relevant parts of the GEOS-Chem forward model up through version v9. The GEOS-Chem adjoint model has been developed and widely used to constrain sources of emission such as dust (Wang et al., 2012), ammonia (Zhu et al., 2013), CO (Kopacz et al., 2009, 2010; Jiang et al., 2011), CH_4 (Wecht et al., 2012, 2014), and to investigate pollution transport (e.g., Zhang et al., 2009; Kopacz et al., 2011).

The 4-D variational data assimilation technique is used with the GEOS-Chem adjoint model to combine observations and models to calculate an optimal estimate of emissions. A range of emissions are constructed using control variables, $\boldsymbol{\sigma}$, to adjust the vector of model emissions via application as scaling factors with elements $\boldsymbol{\sigma} = \frac{E}{E_a}$, where E and $E_\mathbf{a}$ are posteriori and prior BC emission vectors, respectively. This method of inverse modeling seeks $\boldsymbol{\sigma}$ that minimizes the cost function, J, presented by:

$$J = \frac{1}{2}\sum_{c\in\Omega}(Hc - c_{\text{obs}})^T \mathbf{S}_{\text{obs}}^{-1}(Hc - c_{\text{obs}}) + \frac{1}{2}\gamma_{\text{r}}(\sigma - \sigma_a)^T \mathbf{S}_a^{-1}(\sigma - \sigma_a), \quad (1)$$

where c is the vector of species concentrations mapped to the observation space by H, the observation operator, c_{obs} is the vector of species observations, σ_a is the prior estimate of the scaling factors, $\mathbf{S}_{\text{obs}}$ and $\mathbf{S}_a$ are error covariance estimates of the observations and scaling factors, respectively, and Ω is the domain over which observations are available. The first term of the cost function in Eq. (1) is the observation term, which is the total prediction error incurred for departure of model predictions from the observations. The second term, the a priori term or penalty (background) term, is the penalty incurred for departure from the prior emissions. Here $\mathbf{S}_a$ is assumed to be diagonal, and the significance of the prior information is more of a smoothness constraint than a rigorous estimate of prior uncertainty (Rodgers, 2000). γ_{r} is a regularization parameter, which used to balance the two terms (Hansen, 1998; Henze et al., 2009). We will discuss the contributions of the penalty term in Sect. 4.2.

ACPD
14, 28385–28452, 2014

Overall, the minimum value of the cost function balances the objectives of improving model performance while ensuring the model itself remains within a reasonable range (as dictated by $\mathbf{S}_a^{-1}$) of the initial model. The minimum of the cost function is sought iteratively using the quasi-Newton L-BFGS-B algorithm (Zhu et al., 1994; Byrd et al., 1995). This approach requires at each iteration the gradients of the cost function with respect to the emission scaling factors, which are calculated with the GEOS-Chem adjoint model.

2.5 Adjoint forcing

The gradient of the cost function with respect to species concentrations is referred to as the adjoint forcing. The OMI AAOD column observations contain the combined effects of all absorbing aerosols, dominated by both BC and dust. For constraining BC alone, we must calculate a forcing that is the gradient of the cost function with respect to BC alone. Here we consider four ways to formulate this adjoint forcing. For these comparisons, we only consider the observation term of the cost function, i.e., the penalty term in the cost function is not included.

a. Vertically resolved BC AAOD based on model. In this case, the adjoint forcing is the difference between simulated BC AAOD and observed BC AAOD at each vertical layer. Here the observed BC AAOD at each vertical layer is derived from the OMI AAOD using the ratio of vertically resolved BC AAOD to column AAOD simulated in the a priori model,

$$\mathbf{T}_{\mathrm{OMI}} \frac{\tau^a_{\mathrm{BC},l}}{\mathbf{T}^a_{\mathrm{GC}}} \tag{2}$$

where $\tau_{\mathrm{BC},l}$ is the modeled BC AAOD at layer l, $\mathbf{T}_{\mathrm{OMI}}$ is the observed column AAOD, superscript a indicates the a priori parameters, and the modeled column AAOD

$$\mathbf{T}_{\mathrm{GC}} = \mathbf{T}_{\mathrm{BC}} + \mathbf{T}_{\mathrm{OC}} + \mathbf{T}_{\mathrm{Dust}}. \tag{3}$$

ACPD
14, 28385–28452, 2014

The observation term of the cost function can be written as:

$$J = \frac{1}{2}\sum_{i}^{N}\sum_{l=1}^{L}\left(\tau_{\mathrm{BC},l,i} - \mathbf{T}_{\mathrm{OMI},i}\frac{\tau^{a}_{\mathrm{BC},l,i}}{\mathbf{T}^{a}_{\mathrm{GC},i}}\right)^{2}\cdot\mathbf{S}^{-2}_{\mathrm{OMI},i}, \quad (4)$$

where L is the top of atmosphere and N is the total number of all the observations. If we treat, for simplicity, the ratio $\frac{\tau^{a}_{\mathrm{BC},l}}{\mathbf{T}^{a}_{\mathrm{GC}}}$ as a constant, the gradient of the cost function with respect to the BC concentration at vertical layer l will be

$$\frac{\partial J}{\partial \mathrm{BC}_{l}} = \frac{\partial \tau_{\mathrm{BC},l}}{\partial \mathrm{BC}_{l}}\cdot\left(\tau_{\mathrm{BC},l} - \mathbf{T}_{\mathrm{OMI}}\frac{\tau^{a}_{\mathrm{BC},l}}{\mathbf{T}^{a}_{\mathrm{GC}}}\right)\cdot\mathbf{S}^{-2}_{\mathrm{OMI}}. \quad (5)$$

b. Column BC AAOD based on model. In this case, the adjoint forcing is the difference between the total simulated BC AAOD and observed BC AAOD in each column. The observed BC AAOD column is derived from the OMI AAOD column and the ratio of simulated column BC AAOD to simulated total column AAOD from the a priori simulation:

$$\mathbf{T}_{\mathrm{OMI}}\frac{\mathbf{T}^{a}_{\mathrm{BC}}}{\mathbf{T}^{a}_{\mathrm{GC}}}, \quad (6)$$

Thus of cost function is then:

$$J = \frac{1}{2}\sum_{i}^{N}\left(\mathbf{T}_{\mathrm{BC},i} - \mathbf{T}_{\mathrm{OMI},i}\frac{\mathbf{T}^{a}_{\mathrm{BC},i}}{\mathbf{T}^{a}_{\mathrm{GC},i}}\right)^{2}\cdot\mathbf{S}^{-2}_{\mathrm{OMI},i}. \quad (7)$$

The gradient of the cost function with respect to BC concentration at layer l will be

$$\frac{\partial J}{\partial \mathrm{BC}_{l}} = \frac{\partial \tau_{\mathrm{BC},l}}{\partial \mathrm{BC}_{l}}\cdot\left(\mathbf{T}_{\mathrm{BC}} - \mathbf{T}_{\mathrm{OMI}}\frac{\mathbf{T}^{a}_{\mathrm{BC}}}{\mathbf{T}^{a}_{\mathrm{GC}}}\right)\cdot\mathbf{S}^{-2}_{\mathrm{OMI}}. \quad (8)$$

ACPD
14, 28385–28452, 2014

c. Total OMI AAOD. The adjoint forcing is the difference between simulated total AAOD and observed OMI AAOD. The observation term of the cost function can then be written as:

$$J = \frac{1}{2}\sum_{i}^{N}(\mathbf{T}_{\mathrm{GC},i} - \mathbf{T}_{\mathrm{OMI},i})^2 \cdot \mathbf{S}_{\mathrm{OMI},i}^{-2} \quad (9)$$

Based on Eq. (3), the gradient of the cost function with respect to BC concentration at layer *l* will be

$$\frac{\partial J}{\partial \mathrm{BC}_l} = \frac{\partial \tau_{\mathrm{BC},l}}{\partial \mathrm{BC}_l} * (\mathbf{T}_{\mathrm{BC}} + \mathbf{T}_{\mathrm{OC}} + \mathbf{T}_{\mathrm{Dust}} - \mathbf{T}_{\mathrm{OMI}}) \cdot \mathbf{S}_{\mathrm{OMI}}^{-2}. \quad (10)$$

d. Column OMI AAOD with BC_flagged (OMI_AAOD_BC). The OMI OMAERUV retrievals also identify retrievals for which the retrieval algorithm relied upon the presence of carbonaceous aerosols with BC flags. Using only these retrievals, the adjoint forcing will be the direct difference between simulated BC AAOD and observed OMI AAOD with BC flags, and the observation term of the cost function can be written as:

$$J = \frac{1}{2}\sum_{i}^{N}(\mathbf{T}_{\mathrm{BC},i} - \mathbf{T}_{\mathrm{OMI\ BC},i})^2 \cdot \mathbf{S}_{\mathrm{OMI\ BC},i}^{-2}. \quad (11)$$

Based on Eq. (3), the gradient of the cost function with respect to BC concentration at the layer *l* will be

$$\frac{\partial J}{\partial \mathrm{BC}_l} = \frac{\partial \tau_{\mathrm{BC},l}}{\partial \mathrm{BC}_l} \cdot (\mathbf{T}_{\mathrm{BC}} - \mathbf{T}_{\mathrm{OMI\ BC}}) \cdot \mathbf{S}_{\mathrm{OMI\ BC}}^{-2}. \quad (12)$$

The implications of the different cost function formulations will be described in Sect. 4.1.

ACPD
14, 28385–28452, 2014

3 Impacts of BC anthropogenic emission uncertainties

In this section, we quantify the extent to which differences in anthropogenic emission inventories contribute to uncertainties in simulated surface BC and AAOD. Here, the SEAC^{4}RS emission inventory is appended to the MEIC emission inventory outside of China for the Southeast Asian nested simulation (MEIC_SEAC^{4}RS). Figure 4 shows the impact of different BC anthropogenic emission inventories on simulated surface BC concentrations and comparisons to in situ measurements over China (Zhang et al., 2008; Cao et al., 2009). The monthly and daily ground-based measurements at sites representative of four different regions are shown: northern China (Gucheng, GUC), northeastern China (Longfengshan, LFS), southern China (Nanning, NAN), and mid-western China (XiAn, XIA). Generally, the modeled and observed BC concentrations are higher in winter than in summer. In addition to enhanced anthropogenic emissions during the winter (Fu et al., 2012), the Asian summer monsoon plays an important role in this seasonal cycle by reducing aerosol concentrations in the summer over China (Zhang et al., 2010). Though the model simulation is able to capture the seasonal variability, it underestimates surface BC concentration at the urban sites, such as GUC, NAN, and XIA, with all of these anthropogenic emission inventories, except at NAN, where the SEAC^{4}RS inventory leads to values as high or higher than observed, but the seasonal variation has not yet been reproduced. With the INTEX-B and MEICS inventory, though the surface BC concentrations are underestimated at some background and rural sites (Fu et al., 2012; Wang et al., 2013), the simulated BC surface concentrations at the rural site of LFS are quite comparable to the observation, especially the seasonal variations. The INTEX-B and MEIC inventories improve the BC concentrations in winter with the inclusion of monthly variability over China compared to the inventories of Bond and SEAC^{4}RS.

The spatial distributions of simulated surface BC concentrations using MEIC_SEAC^{4}RS and INTEX-B inventories are compared to the in situ observation at 20 sites over Southeast Asia for April and October 2006 in Fig. 5. The east to

ACPD
14, 28385–28452, 2014

west gradient in China and the north to south gradient in India are not well reproduced by the model, where the simulated BC concentrations are much lower over eastern China and the IGP for both April and October, especially for the urban areas since the model is unable to resolve individual urban hot spots (Fu et al., 2012).

Figure 6a shows the differences in monthly average AAOD between the model using the MEIC_SEAC^{4}RS inventory and OMI (former minus latter) for April and October 2006. GEOS-Chem underestimates AAOD compared to OMI across broad areas of Southeast Asia in April, especially eastern China and the IGP. In October, AAOD is underpredicted over northern China while it is over predicted over eastern China and most of South Asia. Corresponding OMI data counts towards the monthly average at each grid cell are shown in Fig. 6b. In general, more data are available over northern China and India. We note that the data counts are much lower in October compared to April over southern China and the Indo China Peninsular, where the observations are overestimated. Sparse OMI observations over these areas may result in apparent high or low biases. If we only take into account the OMI_AAOD_BC retrievals, the differences and corresponding OMI data counts for April and October are shown in Fig. 7. The spatial distributions are quite similar to those using all AAOD observations shown in Fig. 6, but with much larger negative differences over Asia in April and over northern China and IGP in October. The data counts are also smaller when only considering the OMI_AAOD_BC observations, especially over the dust source regions and downwind areas in April and broad areas over South Asia in October.

We also compared the observed to simulated AAOD using different emission inventories (figures not shown here). The simulated AAOD is comparable using INTEX-B and MEIC emission inventories over eastern China, while it is much lower than the OMI column retrieval using the inventories of Bond and SEAC^{4}RS. With the SEAC^{4}RS inventories, the simulated AAOD over the IGP shows enhancements compared to that using Bond and INTEX-B inventories.

ACPD
14, 28385–28452, 2014

4 Uncertainties of observation and penalty terms

4.1 Adjoint forcing

As described in Sect. 2.5, there are four methods to calculate the adjoint forcing owning to different ways of deriving an "observed" BC AAOD. In order to quantify the impact of using these different observation operators, we perform sensitivity experiments. For these tests, only the observation term is considered in the cost function (i.e., the penalty term is not included), and we use the same anthropogenic emission inventory (MEIC_SEAC^{4}RS) as the prior emissions for each test. Figure 8 shows the results of the differences between optimized and prior anthropogenic BC emissions based on the four adjoint forcing methods.

Qualitatively, there are many noticeable differences between the optimization results using the different formulations of the observation operator. In April, enhanced anthropogenic BC emissions are shown over broad areas using all four methods. However, slight reductions appear over eastern China and southern India when using method (b), (c) and (d). In particular, method (c) results in lower posterior emissions over China. The results of methods (c) and (d) are quite consistent except the enhancements of posterior emissions over southern India occur using method (d). Similarly, although the four optimized patterns are quite consistent in October, much larger areas of BC emissions reduction result from using method (c). The reductions of method (d) are similar to that of method (c) over eastern China, while quite different over India with significantly enhanced posterior emissions.

The differences in results are related to different assumptions implicit in the various forms of the cost function considered. Both method (a) and method (b) depend on the relative ratio of BC to other absorbing aerosol (e.g. dust, OC) in the model. Further, method (a) introduces a stronger dependency on the GEOS-Chem prior vertical distribution, since the observation operator includes three dimensions with all vertical layers, compared to the column based method (b). Since there are more observations over IGP and northeastern China in April, this stronger constraint may enhance

ACPD
14, 28385–28452, 2014

the negative forcing due to the model underestimation, which leads to increasing emissions. Since, through the adjustment of the OMI data to generate the OMI_GC product, we have already used the GEOS-Chem prior information on the aerosol vertical distribution, it seems preferable to adopt a column-based approach for the assimilation. Though both method (b) and method (c) are based on the column AAOD, the former assumes that the relative contributions of BC to total AAOD in the model is correct, while the latter assumes that absolute contributions of OC and dust are correct. The simulated total AAOD might not be equivalent to the observed AAOD after optimization in both method (a) and method (b) since the adjoint forcing only accounts for the BC AAOD. In addition, the results would highly depend on the model performance in simulating the ratio between BC and other absorbing aerosol. There are no significant biases for the GEOS-Chem simulated faction of coarse model dust mass (Wang et al., 2012; Philip et al., 2014), which suggests that the simulated dust AAOD fraction is likely unbiased. However the simulated mass of both BC and OC in GEOS-Chem are biased low (Heald et al., 2005; Fu et al., 2012). We thus adopt method (c), since the strength of the adjoint forcing with respect to BC sources depends upon the BC absolute contribution in AAOD rather than the relative contribution of method (b), which may have less model dependency in simulating the distribution of other aerosols. The major differences between method (c) and method (d) are the available observation data counts, as the data counts of the latter are much fewer than the former. In April, the pattern of optimized emissions using method (c) and method (d) are quite consistent, suggesting that BC AAOD play a dominant role in contributing to the total AAOD. We will adopt method (c) for the following experiments and also discuss method (d) in Sect. 5.4 for comparison.

4.2 Penalty term

The inclusion of a penalty, or background term, in the cost function is a key factor for inverse modeling. It is specified through the prior (background) error covariance matrix, $\mathbf{S}_a$, and a regularization parameter γ_r. In the absence of rigorous statistical information

ACPD
14, 28385–28452, 2014

on the error covariance of the emissions, we assume the errors are uncorrelated and use an L-curve selection criterion to identify an optimal value of γ_r (Hansen, 1998; Henze et al., 2009). The uncertainties of BC are assumed to be 100 % of the maximum BC emissions over the simulation domain. Thus, the optimal values of γ_r are selected to be 0.5 for April and 1.0 for October based on the MEIC_SEAC^{4}RS emission and the adjoint forcing of Eq. (9). The contribution of the penalty term results in smaller adjustments to emissions, as the regularized results prefer smoother solutions than those of the unconstrained inversion tests in Fig. 8. Here we assume a single constant value for $\mathbf{S}_a$ along the diagonal and no off-diagonal terms.

5 Analysis of optimizations

We next proceed to constrain Southeast Asian BC sources using OMI AAOD. The OMI AAOD observations are compared to model estimates from GEOS-Chem nested simulation for April and October 2006 using the difference between simulated total AAOD and observed OMI AAOD (i.e., Eq. 9). Tens of thousands of OMI retrievals per month are available for the assimilation, but not all of the retrievals are usable. In the presence of cirrus clouds, retrievals errors are significant. The effect of optically thin cirrus is similar to that of subpixel cloud contamination. As plumes of dust or smoke aerosol drift away from their source regions, they become mixed with clouds. This problem is particularly evident over the oceans, which are frequently covered with thin cirrus and fair-weather cumulus clouds. Generally, the retrieved AAOD shows a reduced coverage especially over the oceans due to cloud contamination and the effects of sun glint (Torres et al., 2007). Thus, quality and diagnostic flags are defined to classify and filter the retrievals. In October, only observations north of 5° N are included for data assimilation to minimize contributions of biomass burning from Indonesian fires.

ACPD
14, 28385–28452, 2014

5.1 Optimized emissions

Considering the performances of the four emission inventories discussed in Sect. 2.3, the following optimized results will mainly focus on using the MEIC_SEAC^{4}RS and INTEX-B inventories. The prior and posterior (optimized) BC emissions from anthropogenic sources are shown in Fig. 9. Overall, the results show an enhancement in BC emissions over broad areas of Southeast Asia, with adjustments that are seasonally and spatially heterogeneous. This is consistent with the top-down constraints on BC emissions based on ground-base measurements by Fu et al. (2012), which also show that the BC emissions are greatly enhanced across broad areas of China, in particular northern and central China and the megacity clusters. In April, either using MEIC_SEAC^{4}RS or INTEX-B inventories, large increases of up to a factor of 3–5 are shown after optimization. The largest enhancements occur sharply in eastern China and the IGP in April by up to a factor of five (Fig. 9). Other large increases are located in South Asia, northeastern and northwestern China. There is a small decrease in anthropogenic BC in part of southwestern China. That is quite different from the inversion results based on AOD by Xu et al. (2013), wherein the optimized anthropogenic BC emissions are reduced by 9.1 % over China, even though the prior BC anthropogenic emissions that they used are from Bond et al. (2004, 2007), which much lower than what we used. The dust scheme had not yet been updated and modified in Xu et al. (2013) following the revised particle size distribution suggested in Zhang et al. (2013). Thus it is possible that overestimated dust and AOD projected a model bias onto adjustments of emissions of all type of aerosols over dust regions and downwind areas, such as eastern China. However, the adjustments of anthropogenic BC emissions before and after optimization in October are different than those in April (Fig. 10). The optimization of anthropogenic emissions yields a slight reduction ($1 \sim 5$ %) over central India and part of southern China and an increase by $10 \sim 50$ % over eastern and northern China, as well as northwestern India.

ACPD
14, 28385–28452, 2014

Though the adjusted patterns of optimized BC emission are basically comparable by using MEIC_SEAC^{4}RS and INTEX-B inventories, significant differences are located over India and eastern China (Fig. 11). We also note that the differences in the optimized results are almost the same as those of the prior emissions between MEIC_SEAC^{4}RS and INTEX-B inventories. The ratio between their posterior differences and prior differences (see Fig. 11, right column) shows that the optimization increases their differences, relative to the prior, over broad areas over China and India up to a factor of three in April, with only slight decreases over south India. In October, optimization decreases the posterior differences between MEIC_SEAC^{4}RS and INTEX-B emission inventories relative to the prior by 10–20 % over southern and most of India. Areas where prior differences are increased/reduced are consistent with the areas where the emissions increase/decrease after optimization (see Fig. 10). This suggests that absolute errors in the prior emissions may be larger than the relative prior uncertainty percentages considered here.

In addition to the changes in the magnitude of the emissions, it is important to consider how much the inversion has reduced uncertainty in the emissions. A new method based on the Broyden–Fletcher–Goldfarb–Shanno (BFGS) algorithm is used to estimate the posterior uncertainty (Bousserez et al., 2014). The posterior error reductions are up to 30 and 15 % in April and October over the IGP and eastern China, where the anthropogenic emission enhancements were the largest (Figs. 9 and 10). The prior errors do not change across broad areas, where the changes of optimized emissions are relatively smaller.

While the most substantial adjustments are made to anthropogenic emissions, biomass burning emission are also adjusted. The most significant increases are over South Asia and eastern Europe in April, especially, the indo-China peninsula and eastern Russia (figures not shown). The optimized biomass burning emissions in October have the largest enhancements are over south Borneo and Sumatra. Similar to the optimized anthropogenic emission, there is also not much change for the optimazed biomass burning emission throughout India and and indo-China peninsula in October.

ACPD
14, 28385–28452, 2014

To examine the impacts of different prior anthropogenic inventories on optimized biomass burning emissions, we consider the following ratios:

$$\frac{\Delta\text{MEIC\_SEAC4RS}_{\text{GFED3}} - \Delta\text{MEIC\_SEAC4RS}_{\text{GFED2}}}{\text{GFED3} - \text{GFED2}}. \quad (13)$$

Equation (13) shows how changes in anthropogenic emissions during the optimization compare when using two different biomass burning inventories, relative to the difference in these biomass burning inventories themselves. Large values of this ratio indicate regions where top-down constrains on anthropogenic emissions are very sensitive to errors in the prior biomass burning inventories. Thus, the changes in optimized anthropogenic emissions based on GFED v2 and GFED v3 (denominator of Eq. 13) are more sensitive to the differences between GFED v2 and GFED v3 over eastern China and southern IGP (Fig. 12).

5.2 Optimized BC AAOD

The largest uncertainty reductions are obtained over eastern China and the IGP, so here we consider AAOD in these regions alone. Figure 13 shows the observed and simulated BC AAOD over eastern China (105–125° E, 20–45° N) before and after optimization in green along with linear line slope equation and correlation R^2. Here the observed BC AAOD is derived from the OMI AAOD and the prior ratio of simulated BC AAOD vs. total AAOD. The prior BC AAOD is misrepresented and underestimated compared to observation over eastern China, especially in April. The low biases of the prior slopes are improved after optimization in April and October by 132 and 11 %, respectively. Similar to the optimized BC concentrations, the improvements in October after optimization are less significant than in April. There are only slight changes in correlation coefficients, which may due to the large number of samples in both spatial and temporal dimensions across which variations are not in the same directions. In the IGP area, which we define as (70–90° E, 23–32° N), the low biases of prior BC AAOD are much larger than those in eastern China (Fig. 14). The values of most observed BC

ACPD
14, 28385–28452, 2014

AAOD are lower than 0.3 and the slopes are 0.22 and 0.28 in April and October. After optimization, the slope increase by 155 % and the correlation coefficients change from 0.2 to 0.25 in April. In October, there is a 32 % increase in slope and the correlation coefficient doubles but still remains small (from 0.06 to 0.12).

Though slopes improve after optimization for both eastern China and India, they still show considerable lower biases. This results, in part, from constraints of the penalty term. Additionally, we note that many prior AAOD values are very small and close to zero. These are hard for the optimization routine to adjust significantly in the areas where the values of prior emission are very small or close to zero. Since the optimization scheme is based on the use of emissions scaling factors, large gradients with respect to BC concentrations will result in small gradients with respect to emissions scaling factors in locations with small emissions. To test how much this formulation restricts the inversion, a sensitivity experiment was performed assuming uniform prior emissions in all grid boxes. This framework is able to improve this problem by enhancing the small prior emission and prior AAOD to much larger values, resulting in larger posterior AAOD after optimization. However, the spatial distributions and gradients of anthropogenic emissions are not reproduced, especially the large emissions are not located in known urban areas. Alternatively, instead of using scaling factors, $\boldsymbol{\sigma}$, the BC emissions themselves could be used as the control variables in the cost function. Another sensitivity experiment is performed for April 2006, inverting for emissions rather than emissions scaling factors. Figure 15 shows the total emissions (sum of anthropogenic, biofuel, and biomass burning emissions) after optimization using the scaling factor (Fig. 15a) and emission based (Fig. 15b) approaches. Using the emission based approach, adjustments of emissions are significant in areas where the prior emission are very small or close to zero. The optimized emissions over the larger prior source areas, such as northeastern China and the middle IGP, are relative smaller than those using the scaling factor based approach. These sensitivity tests demonstrate the value of using the prior emissions inventories, either explicitly or implicitly through scaling

ACPD
14, 28385–28452, 2014

factors, in terms of constraining the magnitude of known sources, and the downside in terms of the difficulty in introducing new sources through the inversion.

We also evaluate (Fig. 16) the prior and posterior simulated AAOD against the OMI and AERONET daily average AAOD at 4 sites where there are available measurements during the periods of April and October 2006 (see the red sites in Fig. 2): Beijing (BJ) in China, Kanpur (KP) and Gandhi_College (GH) in India, and Mukdahan (MD) in Thailand. The daily average GEOS-Chem model results and OMI AAOD are sampled according to the AERONET observations at the locations of the 4 sites. At the Beijing site, the prior model AAOD estimates driven either by MEIC_SEAC^{4}RS or INTEX-B inventories are underestimated by a factor of ~ 2, while the posterior AAOD are more comparable to the observations in April. In terms of temporal variability, the model is able to capture some features of peaks after optimization. At the two sites in India, only a few measurements are available in late April, but the magnitudes are close to OMI observation. The optimized results using the MEIC_SEAC^{4}RS inventory shows great improvements compared to the prior AAOD. However, the optimized AAOD using the INTEX-B inventory still shows negative biases. The differences in optimized AAOD between using INTEX-B and MEIC_SEAC^{4}RS come from their prior differences in AAOD. This again demonstrates that the posterior optimization results are not independent of the prior emission inventories, consistent with the estimated reduction in posterior error shown in Fig. 10. At the site of Gandhi_College (GH) and Mukdahan (MK) there are large differences between the OMI and AERONET AAODs; the magnitudes of the OMI AAODs are much lower than those from AERONET, even close to zero on some days. Koch et al. (2009) compared the AERONET and OMI retrievals of AAOD at AERONET sites. The results showed that the two retrievals broadly agree with each other, but that the OMI AAOD is much smaller over Southeast Asia. In our study, only a few OMI AAOD pixels are available in Thailand site (MK) (Fig. 6); these limited and sparse observations do not provide enough information to robustly constrain emissions in this region.

ACPD
14, 28385–28452, 2014

5.3 Optimized surface BC concentrations

As mentioned before, the prior surface BC concentrations are underestimated in most of the urban and rural sites over China. Figure 17 shows the spatial distribution of optimized surface BC concentrations compared to in situ measurements at 20 sites in Southeast Asia. The largest in situ BC concentrations observed over eastern China and the IGP, which are densely populated, industrialized areas, are now reproduced well by the optimized simulation. After optimization, the spatial gradients of the observed BC concentrations are captured by the model: high in the east and low in the west for China, and high in the north and low in the south for India. Using the MEIC_SEAC^{4}RS inventory for the prior emissions, the optimized spatial distributions are better simulated than when than using the INTEX-B inventory. In particular, the simulated BC concentrations are much closer to the observations over the IGP after optimization. The scatter plots in Fig. 18 show the correlations of BC concentrations from surface observations and GEOS-Chem before (blue) and after (red) optimization. Initial negative biases are shown in both April and October. The linear regression slope increases by more than a factor of four in April. However, the modeled BC concentrations at most of the sites only slightly change after the optimization in October, which result in a much smaller improvement in the regression slope (21 %). The correlation coefficients increase by 0.04 to 0.08 after optimization, such small improvement may be owing to the sparse spatial distributions of the observational sites.

More specific site-by-site comparisons between model and observations are shown in Fig. 19. Although the optimized BC surface concentrations are enhanced in April, overestimation occurs in some eastern sites over China. In October, the low biases are corrected both in the urban sites and rural sites, especially the eastern rural sites in China. However, there is a persistent negative bias in most sites after optimization in October. Due to the very low prior emissions, the optimization has less impact on the western sites over China. The GEOS-Chem prior simulation underestimates surface BC concentrations in all the urban sites and coastal sites over India in April

ACPD
14, 28385–28452, 2014

(Fig. 17). While the optimization enhances the BC sources and surface concentration, it still shows a negative bias in most of sites over India, especially the urban sites. The smaller improvement in coastal sites is not only due to the low prior emissions but also the large uncertainties of AAOD retrieval for low aerosol amounts over the ocean.

Given the stark contrast between the inversion results in April and October, we also conducted the optimization for two additional months in winter (January) and summer (July) season using MEIC_SEAC^{4}RS as the prior inventory. In January, the anthropogenic emissions show enhancements over the IGP and parts of western and northern China and slight decreases over southern India and eastern and southern China (figures not shown here), which results in increasing the surface BC concentrations in XIA and LFS sites while decreasing concentrations in the sites of GUC and NAN (see Fig. 4). In July, there is no significantly change for the surface BC concentrations after optimization owing to very sparse observation in July over eastern China. From this seasonal comparison, it appears that the BC anthropogenic emissions are not always underestimated during the year. The largest underestimations across the whole region of Southeast Asia occur in April. The underestimated regions are mainly over IGP and northern China in both January and October. The slight overestimates are indicated over southern India and part of eastern China in January as well as northern China in July.

Discrepancies vs. surface observations might also relate to model representational error incurred by comparing ~ 50 km gridded estimates to in situ BC measurements, which likely have finer length-scales of variability (Wang et al., 2013). We investigate the impacts of model resolution by considering approaches for downscaling the model simulations. One approach is to use high-resolution population datasets to redistribute primary aerosol concentrations (e.g., Krol et al., 2005; UNEP, 2011; Silva et al., 2013). Based on a finer resolution population density dataset, a parameterization of the urban increment for non-reactive primary emitted anthropogenic BC and organic matter has been developed and tested for coarse resolution air quality model. This method does not alter concentrations at rural sites since it assumes that re-

ACPD
14, 28385–28452, 2014

sults at coarse resolution only represent the rural (background) sites. According to this method, we used a high-resolution ($1/24^\circ \times 1/24^\circ$) population dataset of Gridded Population of the World, Version 3 (GPWv3, http://sedac.ciesin.columbia.edu/data/set/gpw-v3-population-density-future-estimates) to downscale and adjust the simulated BC concentration at urban sites (defined locations where population density exceeding 600 km^{-2}). The scatter plots (Fig. 18b) show that, on average, the application of population downscaling improves the performance of the modeled results compared to the non-adjusted BC concentrations in April for both the prior and posterior simulations, although low biases remain in each. It does not make any change in the slope in October after applying the population parameterization, and correlation is degraded. Downscaled estimates at only two sites (LIA and NAN) show enhancements, the rest are not impacted.

To more directly investigate the impact of model resolution, it would be ideal to compare the results of the present simulations to higher resolution simulations with the same model (e.g., Punger and West, 2013). While this is not currently an option for this model version, we can conduct GEOS-Chem simulations at a coarser resolution (2° latitude $\times$ 2.5° longitude) and make inferences about the role of resolution errors. Figure 20 shows the resolution errors in estimated surface BC concentrations in the coarse resolution results ($2^\circ \times 2.5^\circ$) with respect to fine resolution simulations ($0.5^\circ \times 0.667^\circ$). The resolution error exceeds 20 % across broad areas, and even up to 300 % over the IGP and part of southeastern Asia. The surface BC concentrations are much lower using coarse resolution over the major source regions, in particular the IGP, where the resolution error is more than 3. This is likely owing to coarse grid boxes not describing the sharp gradient between high concentrations in the valley and low concentrations in the mountain. The optimized surface BC concentrations from our $0.5^\circ \times 0.667^\circ$ simulations are underestimated by a factor of 2–3 at the IGP sites compared to in situ measurements. Punger and West (2013) show that the percent difference between all-cause mortality estimates at 12 km resolution and at coarser resolutions of 36 and 96 km for BC is $\sim$ 9 % and $\sim$ 23 % respectively. Assuming that model skill at estimating

ACPD
14, 28385–28452, 2014

variations in concentrations at the scales of the in situ measurements is similar to that for estimating exposure based on highly resolved populations distribution, we can extrapolate from the results of Punger and West (2013) that the resolution errors in the $0.5^{\circ} \times 0.667^{\circ}$ simulation, relative to the scale of the measurements, is a bit less than the resolution error in the $2^{\circ} \times 2.5^{\circ}$ simulation relative to the $0.5^{\circ} \times 0.667^{\circ}$ simulation. Thus, the former may be as large as a factor of ~ 2.5 in individual grid cells.

5.4 Comparisons using OMI_AAOD_BC

A subset of the OMI retrievals (OMI_AAOD_BC) represents the presence of carbonaceous aerosols. Using only these retrievals for the inversion, the differences between prior and posterior (later minus former) BC anthropogenic emissions using MEIC_SEAC^{4}RS inventory are shown in Fig. 21. Compared to Fig. 9 and Fig. 10, there are similar signs of emissions adjustments over most of Southeast Asia except in October over India where reductions are not shown in the posterior emissions due to fewer available observations in the OMI_AAOD_BC data subset. Moreover, the magnitudes of enhanced emissions in April are much larger if we use only the OMI_AAOD_BC retrievals. This also results in larger posterior surface BC concentrations (figures not shown) in some area and AAOD that improve the underestimates in a few sites when compared to the ground-base measurements and AERONET observation. However, the differences are not obvious in October and the improvements in April are neither significant nor widespread. Considering there are less observations available using OMI_AAOD_BC, especially in October and other summer month (e.g. July), and that it does not change the major conclusions compared to using OMI AAOD, using OMI AAOD is recommended.

ACPD
14, 28385–28452, 2014

6 Summary and discussions

In this study, we used space-based observations of absorbing aerosol optical depth (AAOD) from the OMI instrument to constrain BC monthly average emissions for April and October 2006, with the GEOS-Chem model and its adjoint. First, we evaluated the model simulated BC concentrations using four different anthropogenic emission inventories. The differences in these inventories exceeded 100 % across broad areas of Southeast Asia. For each of the four emission inventories, the simulated surface BC concentrations had low biases compared to the available surface observations in most urban sites in Southeast Asia.

The adjoint model was used to perform 4-D-Var inverse modeling to constrain BC emissions. After optimization, both anthropogenic and biomass burning emissions were adjusted. Either using the MEIC_SEAC^{4}RS or INTEX-B inventory, the optimized anthropogenic emissions for BC were significantly enhanced over broad areas of Southeast Asia in April compared to the prior emission, with the largest enhancements in eastern China and India IGP of up to a factor of five. From analysis of inversions using different prior biomass burning inventories it was shown that optimized anthropogenic emissions was most sensitive to the prior biomass burning over eastern China and southern IGP. The adjustments in October were smaller than those in April. Inverse modeling in additional months indicated that BC anthropogenic emissions were not always underestimated throughout the year. The largest underestimates occurred in April throughout Southeast Asia. Only slight overestimates were indicated over southern India and eastern China for both January in July. Inversion results were in general similar using either all OMI AAOD or just the OMI_AAOD_BC. In October, the posterior anthropogenic emissions yielded a slight reduction ($1 \sim 5$ %) over central India and part of southern China while they increased by $10 \sim 50$ % over eastern and northern China, as well as northwestern India. The uncertainty of the posterior emissions over the IGP and eastern China were estimated to have reduced up to 30 and 15 % in April and October.

ACPD
14, 28385–28452, 2014

After optimization, the low model biases for BC AAOD improved by 132 and 11 % over Southeast Asia in April and October, respectively. In eastern China, these improvements were more significant (143 and 30 % in April and October). The remaining residual error in the simulated OMI AAOD, which was significant in October, particularly in India, may be a consequence of the inverse modeling framework, which had difficulty introducing emissions in locations where the prior emissions were close to zero. This downside may be overcome by performing inversions directly for the emissions, rather than emissions scaling factors.

Results of the inversion were also compared to remote and in situ measurements that were not assimilated. The posterior AAOD were quite comparable to AERONET AAOD observations in April in China; however, large discrepancies remained at the sites over India and Thailand after data assimilation. These residual errors compared to AERONET may be associated with the limited and sparse observations of OMI AAOD in these regions, which themselves were not very consistent with the AERONET AAOD. Low biases of surface BC concentrations were improved or corrected at urban sites and eastern rural sites over China in April, with the linear regression slope between model and observed values increasing by more than a factor of four. However, the adjustments were not strong enough in most sites over India in April and October and over China in October. Moreover, the optimization had less impact on the western sites over China and costal sites over India due to the very low prior emissions and the large uncertainties in AAOD retrieval for low aerosol amounts over ocean. Model resolution error was also an important factor contributing to discrepancies of BC concentrations compared to in situ measurements. Comparison to coarser model simulations and the results of Punger and West (2013) indicates that the resolution errors may be up to a factor of 2.5 in grid cells in regions such as the IGP and part of southeastern Asia.

Overall, this work was the first attempt to formally use the absorbing aerosol products from satellite observation for a BC emissions inversion. Both the simulated AAOD and surface BC concentration showed significant improvements spatially and temporally after data assimilation, especially in April. However, there were still several sources of

ACPD
14, 28385–28452, 2014

uncertainty and limitations of this work worth considering. Aspects such as model error and assumptions made regarding the treatment of the observations and uncertainties in the observations and prior emissions inventories contributed greatly to uncertainties in the optimization results.

Assuming the prior emissions errors were only 100 % limited the magnitude of the emissions adjustments allowed by the inversion. Uncertainties in the emissions were also not likely the only cause of the discrepancy between observed and predicted BC concentrations and AAOD. Textor et al. (2007) found that inter-model differences were only partially explained by differences in emission inventories. Uncertainty in modeled horizontal and vertical transport was known to be largely responsible for the diversity in modeled BC concentrations (Bond et al., 2013). Removal processes also played an important role in affecting the lifetime and concentrations of BC lifted into the free troposphere. The scheme for aerosol scavenging was based on Liu et al. (2001), which did not distinguish between rain and snow. The recent updates by Wang et al. (2011) included corrections to below-cloud and in-cloud scavenging that improved the overestimation of integrated scavenging (Dana and Hales, 1976). Corresponding updates to the wet scavenging in the GEOS-Chem adjoint might also be helpful for improving the optimized results.

The optimizations were sensitive to how model information was used to calculate BC component of the measured AAOD, which alone provided only a constraint on the column concentrations of all absorbing aerosol (i.e., including dust and OC). We have corrected the OMI AAOD by applying the GEOS-Chem simulated aerosol layer height to reduce the differences in the vertical profiles between the model and observation. However, there could be inconsistent treatment of microphysical and optical properties used in the AAOD calculation between the model and OMI retrievals. It is important to realize that BC from most emission sources contained not only elemental and organic fractions (Chow et al., 2009), but also non-soot OC, i.e., brown carbon, that has a significant absorbing component at short wavelengths comparable to elemental carbon absorption (Jacobson, 1999; Kirchstetter et al., 2004; Andreae and Gelencser, 2006;

ACPD
14, 28385–28452, 2014

Hoffer et al., 2006; Magi et al., 2009). It is well known that AAOD is the combined effect from the contributions of all such absorbing aerosols. However, absorbing aerosols in GEOS-Chem only include BC, OC and dust, while the brown carbon has not yet been taken into account in current work. While the attribution of ambient aerosol absorption to BC may be a reasonable approximation in areas dominated by fresh soot emissions, it may lead to misleading estimates of the AAOD when other light absorbing particles were present since the brown carbon contributed 28 % on average of the total absorption at the wavelength of 440 nm (Bahadur et al., 2012). It undoubtedly resulted in overestimation of BC emissions after optimization in the areas where brown carbon and other absorbing aerosols were considered in the observed AAOD.

Lastly, it is well known that the quality of the observation data plays the most important role in data assimilation. Although the OMI AAOD retrieval provided much better spatial and temporal coverage than the remote sensing measurements, such as AERONET, we noted that there were large discrepancies between OMI AAOD and AERONET observation in some areas, especially in October (see Fig. 16). Normally, the OMAERUV retrievals were more reliable over land than over water since the ocean surface reflectance show distinct angular and spectral variations. The major factor affecting the quality of the OMI aerosol product was sub-pixel cloud contamination due to the relatively large footprint of the OMI observations (Torres et al., 1998). Satheesh et al. (2009) demonstrated the potential of multisatellite analysis of A-train data to improve the accuracy of retrieved aerosol products and suggested that a combined OMI-MODIS-CALIPSO retrieval had potential to further improve assessments of aerosol absorption, which would possible enhance the observation quality in data assimilation. Important algorithm improvements have been implemented in the current OMAERUV algorithm and the carbonaceous aerosol model was replaced with a new model that accounted for the presence of OC while the previous aerosol model only assumed black carbon as the absorbing component (Jethva and Torres, 2011). Recently, other improvements included the development of CALIOP-based aerosol layer height climatology and the use of AIRS carbon monoxide real time observations to distinguish

ACPD
14, 28385–28452, 2014

smoke from dust type aerosols, which improved the retrieval performance by 5–20 % (Torres et al., 2013). Using the updated OMAERUV when it becomes available will likely improve the optimization results in future work.

The Supplement related to this article is available online at doi:10.5194/acpd-14-28385-2014-supplement.

Acknowledgements. This work was supported from Environmental Protection Agency-STAR grant RD-83503701-0. Although the research described in the article has been funded wholly or in part by the US EPA's STAR program through grant (RD-83503701-0), it has not been subjected to any EPA review and therefore does not necessarily reflect the views of the Agency, and no official endorsement should be inferred.

References

Ackerman, A. S., Toon, O. B., Stevens, D. E., Heymsfield, A. J., Ramanathan, V., and Welton, E. J.: Reduction of tropical cloudiness by soot, Science, 288, 1042–1047, doi:10.1126/science.288.5468.1042, 2000.

Andreae, M. O. and Gelencsér, A.: Black carbon or brown carbon? The nature of light-absorbing carbonaceous aerosols, Atmos. Chem. Phys., 6, 3131–3148, doi:10.5194/acp-6-3131-2006, 2006.

Bahadur, R., Praveen, P. S., Xu, Y., and Ramanathan, V.: Solar absorption by elemental and brown carbon determined from spectral observations, P. Natl. Acad. Sci. USA, 109, 17366–17371, doi:10.1073/pnas.1205910109, 2012.

Beegum, S. N., Moorthy, K. K., Babu, S. S., Satheesh, S. K., Vinoj, V., Badarinath, K. V. S., Safai, P. D., Devara, P. C. S., Singh, S., Vinod, Dumka, U. C., Pant, P.: Spatial distribution of aerosol black carbon over India during pre-monsoon season, Atmos. Environ., 43, 2009, 1071–1078, 2009.

Bey, I., Jacob, D. J., Yantosca, R. M., Logan, A. J., Field, B., Fiore, A. M., Li, Q., Liu, H., Mickley, L. J., and Schultz, M.: Global modeling of tropospheric chemistry with assimilated meteorology: Model description and evaluation, J. Geophys. Res., 106, 23073–23095, 2001.

ACPD
14, 28385–28452, 2014

Bond, T. C. and Bergstrom, R. W.: Light absorption by carbonaceous particles: an investigative review, Aerosol Sci. Tech., 40, 27–67, 2006.

Bond, T. C., Streets, D. G., Yarber, K. F., Nelson, S. M., Woo, J. H., and Klimont, Z.: A technology-based global inventory of black and organic carbon emissions from combustion, J. Geophys. Res.-Atmos., 109, D14203, doi:10.1029/2003JD003697, 2004.

Bond, T. C., Bhardwaj, E., Dong, R., Jogani, R., Jung, S. K., Roden, C., Streets, D. G., and Trautmann, N. M.: Historical emissions of black and organic carbon aerosol from energy-related combustion, 1850–2000, Glob. Biogeochem. Cy., 21, Gb2018, doi:10.1029/2006GB002840, 2007.

Bond, T. C., Doherty, S. J., Fahey, D. W., Forster, P. M., Berntsen, T., DeAngelo, B. J., Flanner, M. G., Ghan, S., Kärcher, B., Koch, D., Kinne, S., Kondo, Y., Quinn, P. K., Sarofim, M. C., Schultz, M. G., Schulz, M., Venkataraman, C., Zhang, H., Zhang, S., Bellouin, N., Guttikunda, S. K., Hopke, P. K., Jacobson, M. Z., Kaiser, J. W., Klimont, Z., Lohmann, U., Schwarz, J. P., Shindell, D., Storelvmo, T., Warren, S. G., and Zender, C. S.: Bounding the role of black carbon in the climate system: a scientific assessment, J. Geophys. Res., 118, 5380–5552, doi:10.1002/jgrd.50171, 2013.

Bousserez, N., Henze, K. D., Perkins, A., Bowman, W. K., Lee, M., Liu, J., Deng, F., Jones, B. A. D: Improved analysis error covariance matrix for high-dimensional variational inversions: application to source estimation using a 3D atmospheric transport model, Q. J. R. Meteorol. Soc., submitted, 2014

Byrd, R. H., Lu, H. P., Nocedal, J., and Zhu, C. Y.: A limited memory algorithm for bound constrained optimization, SIAM J. Sci. Comput., 16, 1190–1208, 1995.

Cao, J. J., Lee, S. C., Chow, J. C., Watson, J. G., Ho, K. F., Zhang, R. J., Jin, Z. D., Shen, Z. X., Chen, G. C., Kang, Y. M., Zou, S. C., Zhang, L. Z., Qi, S. H., Dai, M. H., Cheng, Y., and Hu, K.: Spatial and seasonal distributions of carbonaceous aerosols over China, J. Geophys. Res., 112, D22S11, doi:10.1029/2006JD008205, 2007.

Cao, J. J., Zhu, C. S., Chow, J. C., Watson, J. G., Han, Y. M., Wang, G., Shen, Z., and An, Z. S.: Black carbon relationships with emissions and meteorology in Xi'an, China, Atmos. Res., 94, 194–202, 2009.

Chen, D., Wang, Y., McElroy, M. B., He, K., Yantosca, R. M., and Le Sager, P.: Regional CO pollution and export in China simulated by the high-resolution nested-grid GEOS-Chem model, Atmos. Chem. Phys., 9, 3825–3839, doi:10.5194/acp-9-3825-2009, 2009.

ACPD
14, 28385–28452, 2014

Chin, M., Ginoux, P., Kinne, S., Torres, O., Holben, B. N., Duncan, B. N., Martin, R. V., Logan, J. A., Higurashi, A., and Nakajima, T.: Tropospheric aerosol optical thickness from the GOCART model and comparisons with satellite and sun photometer measurements, J. Atmos. Sci., 59, 461–483, 2002.

Chow, J. C., Watson, G. J., Doraiswamy, P., Chen, W. A., L., Sodeman, A. D., Lowenthal, H. D., Park, K., Arnott, P. W., and Motallebi, N.: Aerosol light absorption, black carbon, and elemental carbon at the Fresno Supersite, California, Atmos. Res., 93, 874–887, 2009.

Cohen, J. B. and Wang, C.: Estimating global black carbon emissions using a top-down Kalman filter approach, J. Geophys. Res.-Atmos., 119, 307–323, doi:10.1002/2013JD019912, 2014.

Cooke, W. F., Liousse, C., Cachier, H., and Feichter, J.: Construction of a $1^{\circ} \times 1^{\circ}$ fossil fuel emission data set for carbonaceous aerosol and implementation and radiative impact in the ECHAM4 model, J. Geophys. Res., 104, 22137–22162, 1999.

Cozic, J., Verheggen, B., Mertes, S., Connolly, P., Bower, K., Petzold, A., Baltensperger, U., and Weingartner, E.: Scavenging of black carbon in mixed phase clouds at the high alpine site Jungfraujoch, Atmos. Chem. Phys., 7, 1797–1807, doi:10.5194/acp-7-1797-2007, 2007.

Dana, M. T. and Hales, J. M.: Statistical aspects of washout of polydisperse aerosols, Atmos. Environ., 10, 45–50, 1976.

Dubovik, O. and King, D. M.: A flexible inversion algorithm for retrieval of aerosol optical properties from Sun and sky radiance measurements, J. Geophys. Res., 105, 20673–20696, 2000.

Dubovik, O., Smirnov, A., Holben, B. N., King, M. D., Kaufman, Y. J., Eck, T. F., and Slutsker, I.: Accuracy assessment of aerosol optical properties retrieval from AERONET sun and sky radiance measurements, J. Geophys. Res., 105, 9791–9806, 2000.

Dubovik, O., Holben, B. N., Eck, T. F., Smirnov, A., Kaufman, Y. J., King, M. D., Tanré, D., and Slutsker, I.: Variability of absorption and optical properties of key aerosol types observed in worldwide locations, J. Atmos. Sci., 59, 590–608, 2002a.

Dubovik, O., Holben, B. N., Lapyonok, T., Sinyuk, A., Mishchenko, M. I., Yang, P., and Slutsker, I.: Non-spherical aerosol retrieval method employing light scattering by spheroids, Geophys. Res. Lett., 29(10), doi:10.1029/2001GL014506, 2002b.

Dubovik, O., Sinyuk, A., Lapyonok, T., Holben, B. N., Mishchenko, M., Yang, P., Eck, T. F., Volten, H., Muñoz, O., Veihelmann, B., van der Zande, W. J., Leon, J.-F., Sorokin, M., and Slutsker, I.: Application of spheroid models to account for aerosol particle nonsphericity in

ACPD
14, 28385–28452, 2014

remote sensing of desert dust, J. Geophys. Res., 111, D11208, doi:10.1029/2005JD006619, 2006.
Eck, T. F., Holben, B. N., Reid, J. S., Dubovik, O., Smirnov, A., O'Neill, N. T., Slutsker, I., and Kinne, S.: Wavelength dependence of the optical depth of biomass burning, urban, and desert dust aerosols, J. Geophys. Res., 104, 31333–31349, 1999.
Fairlie, T. D., Jacob, D. J., Dibb, J. E., Alexander, B., Avery, M. A., van Donkelaar, A., and Zhang, L.: Impact of mineral dust on nitrate, sulfate, and ozone in transpacific Asian pollution plumes, Atmos. Chem. Phys., 10, 3999–4012, doi:10.5194/acp-10-3999-2010, 2010.
Flanner, M. G., Zender, C. S., Randerson, J. T., and Rasch, P. J.: Present-day climate forcing and response from black carbon in snow, Geophys. Res.-Atmos., 112, D11202, doi:10.1029/2006jd008003, 2007.
Forster, P., Ramawamy, V., Artaxo, P., Berntsen, T., Betts, R., Fahey, D., Haywood, J., Lean, J., Lowe, D., Myhre, G., Nganga, J., Prinn, R., Raga, G., Schulz, M., and Dorland, V. R.: Changes in atmospheric constituents and in radiative forcing, in: Climate Change 2007: the Physical Scinece Basis, Contributions of Working Group I to the fourth Assessment Report on the Intergovernmental Panel on Climate Changed, edited by: Solomon, S., Wuin, D., Manning, M., Chen, A., Marquis, M., Averyt, K., Tignor, M., and Miller, H., Cambridge University Press, Cambridge, UK and New York, NY, USA, 2007.
Fu, T.-M., Cao, J. J., Zhang, X. Y., Lee, S. C., Zhang, Q., Han, Y. M., Qu, W. J., Han, Z., Zhang, R., Wang, Y. X., Chen, D., and Henze, D. K.: Carbonaceous aerosols in China: top-down constraints on primary sources and estimation of secondary contribution, Atmos. Chem. Phys., 12, 2725–2746, doi:10.5194/acp-12-2725-2012, 2012.
Giglio, L., van der Werf, G. R., Randerson, J. T., Collatz, G. J., and Kasibhatla, P.: Global estimation of burned area using MODIS active fire observations, Atmos. Chem. Phys., 6, 957–974, doi:10.5194/acp-6-957-2006, 2006.
Giglio, L., Randerson, J. T., van der Werf, G. R., Kasibhatla, P. S., Collatz, G. J., Morton, D. C., and DeFries, R. S.: Assessing variability and long-term trends in burned area by merging multiple satellite fire products, Biogeosciences, 7, 1171–1186, doi:10.5194/bg-7-1171-2010, 2010.
Ginoux, P., Prospero, M. J., Torres, O., and Chin, M.: Long-term simulation of global dust distribution with the GOCART model: correlation with North Atlantic oscillation, Environ. Modell. Softw., 19, 113–128, 2004.

ACPD
14, 28385–28452, 2014

Hakami, A., Henze, K. D., Seinfeld, H. J., Chai, T., Tang, Y., Carmichael, R. G., and Sandu, A.: Adjoint inverse modeling of black carbon during the Asian Pacific Regional Aerosol Characterization Experiment, J. Geophys. Res., 110, D14301, doi:10.1029/2004JD005671, 2005.
Hansen, A. D. A., Rosen, H., and Novakov, T.: The aethalometer – an instrument for the real-time measurement of optical absorption by aerosol particles, Sci. Total Environ., 36, 191–196, 1984.
Hansen, J. and Nazarenko, L.: Soot climate forcing via snow and ice albedos, P. Natl. Acad. Sci. USA, 101, 423–428, doi:10.1073/pnas.2237157100, 2004.
Hansen, J., Sato, M., Ruedy, R., Lacis, A., and Oinas, V.: Global warming in the twenty-first century: an alternative scenario, P. Natl. Acad. Sci. USA, 97, 9875–9880, 2000.
Hansen, J., Sato, M., Ruedy, R., Nazarenko, L., Lacis, A., Schmidt, G. A., Russell, G., Aleinov, I., Bauer, M., Bauer, S., Bell, N., Cairns, B., Canuto, V., Chandler, M., Cheng, Y., Del Genio, A., Faluvegi, G., Fleming, E., Friend, A., Hall, T., Jackman, C., Kelley, M., Kiang, N., Koch, D., Lean, J., Lerner, J., Lo, K., Menon, S., Miller, R., Minnis, P., Novakov, T., Oinas, V., Perlwitz, Ja., Perlwitz, Ju., Rind, D., Romanou, A., Shindell, D., Stone, P., Sun, S., Tausnev, N., Thresher, D., Wielicki, B., Wong, T., Yao, M., and Zhang, S.: Efficacy of climate forcings, J. Geophys. Res., 110, D18104, doi:10.1029/2005JD005776, 2005.
Hansen, P. C.: Rank-Deficient and Discrete Ill-Posed Problems: Numerical Aspects of Linear Inversion, SIAM, Philadelphia, USA, 1998.
Heald, C. L., Jacob, J. D., Park, J. R., Russell, M. L., Huebert, J. B., Seinfeld, H. J., Liao, H., and Weber, J. R.: A large organic aerosol source in the free troposphere missing from current models, Geophys. Res. Lett., 32, L18809, doi:10.1029/2005GL023831, 2005.
Henze, D. K., Hakami, A., and Seinfeld, J. H.: Development of the adjoint of GEOS-Chem, Atmos. Chem. Phys., 7, 2413–2433, doi:10.5194/acp-7-2413-2007, 2007.
Henze, D. K., Seinfeld, J. H., and Shindell, D. T.: Inverse modeling and mapping US air quality influences of inorganic $PM_{2.5}$ precursor emissions using the adjoint of GEOS-Chem, Atmos. Chem. Phys., 9, 5877–5903, doi:10.5194/acp-9-5877-2009, 2009.
Hoffer, A., Gelencsér, A., Guyon, P., Kiss, G., Schmid, O., Frank, G. P., Artaxo, P., and Andreae, M. O.: Optical properties of humic-like substances (HULIS) in biomass-burning aerosols, Atmos. Chem. Phys., 6, 3563–3570, doi:10.5194/acp-6-3563-2006, 2006.
Holben, B. N., Eck, F. T., Slutsker, I., Tanré, D., Buis, P. J., Setzer, A., Vermote, E., Reagan, A. J., Kaufman, J. Y., Nakajima, T., Lavenu, F., Jankowiak, I., and Smirnov, A.: AERONET – a fed-

ACPD
14, 28385–28452, 2014

erated instrument network and data archive for aerosol characterization, Remote Sens. Environ., 66, 1–16, 1998.
Hu, Y., Napelenok, L. S., Odman, T. M., and Russell, G. A.: Sensitivity of inverse estimation of 2004 elemental carbon emissions inventory in the United States to the choice of observational networks, Geophys. Res. Lett., 36, L15806, doi:10.1029/2009GL039655, 2009a.
Hu, Y., Odman, T. M., and Russell, G. A.: Top-down analysis of the elemental carbon emissions inventory in the United States by inverse modeling using Community Multiscale Air Quality model with decoupled direct method (CMAQ-DDM), J. Geophys. Res., 114, D24302, doi:10.1029/2009JD011987, 2009b.
Huneeus, N., Boucher, O., and Chevallier, F.: Atmospheric inversion of SO_2 and primary aerosol emissions for the year 2010, Atmos. Chem. Phys., 13, 6555–6573, doi:10.5194/acp-13-6555-2013, 2013.
Jacobson, M. Z.: Isolating nitrated and aromatic aerosols and nitrated aromatic gases as sources of ultraviolet light absorption, J. Geophys. Res.-Atmos., 104, 3527–3542, 1999.
Jacobson, M. Z.: A physically-based treatment of elemental carbon optics: implications for global direct forcing of aerosols, Geophys. Res. Lett., 27, 217–220, doi:10.1029/1999GL010968, 2000.
Janssen, N. A. H., Lanki, T., Hoek, G., Vallius, M., de Hartog, J. J., Van Grieken, R., Pekkanen, J., and Brunekreef, B.: Associations between ambient, personal and indoor exposure to fine particulate matter constituents in Dutch and Finnish panels of cardiovascular patients, Occup. Environ. Med., 62, 868–877, 2005.
Janssen, N. A., Hoek, G., Simic-Lawson, M., Fischer, P., van Bree, L., ten Brink, H., Keuken, M., Atkinson, R. W., Anderson, H. R., Brunekreef, B., and Cassee, F. R.: Black carbon as an additional indicator of the adverse health effects of airborne particles compared with PM_{10} and $PM_{2.5}$, Environ. Health Persp., 119, 1691–1699, 2011.
Jethva, H. and Torres, O.: Satellite-based evidence of wavelength-dependent aerosol absorption in biomass burning smoke inferred from Ozone Monitoring Instrument, Atmos. Chem. Phys., 11, 10541–10551, doi:10.5194/acp-11-10541-2011, 2011.
Jiang, Z., Jones, B. A. D., Kopacz, M., Liu, J., Henze, K., D., and Heald, C.: Quantifying the impact of model errors on top-down estimates of carbon monoxide emissions using satellite observations, J. Geophys. Res., 116, D15306, doi:10.1029/2010JD015282, 2011.

ACPD
14, 28385–28452, 2014

Johnson, B. T., Shine, P. K., and Forster, M. P.: The semi-direct aerosol effect: impact of absorbing aerosols on marine stratocumulus, Q. J. Roy. Meteorol. Soc., 130, 1407–1422, doi:10.1256/qj.03.61, 2004.

Kirchstetter, T. W., Novakov, T., and Hobbs, V. P.,: Evidence that the spectral dependence of light absorption by aerosols is affected by organic carbon, J. Geophys. Res.-Atmos., 109, D21208, doi:10.1029/2004JD004999, 2004.

Koch, D., Schulz, M., Kinne, S., McNaughton, C., Spackman, J. R., Balkanski, Y., Bauer, S., Berntsen, T., Bond, T. C., Boucher, O., Chin, M., Clarke, A., De Luca, N., Dentener, F., Diehl, T., Dubovik, O., Easter, R., Fahey, D. W., Feichter, J., Fillmore, D., Freitag, S., Ghan, S., Ginoux, P., Gong, S., Horowitz, L., Iversen, T., Kirkevåg, A., Klimont, Z., Kondo, Y., Krol, M., Liu, X., Miller, R., Montanaro, V., Moteki, N., Myhre, G., Penner, J. E., Perlwitz, J., Pitari, G., Reddy, S., Sahu, L., Sakamoto, H., Schuster, G., Schwarz, J. P., Seland, Ø., Stier, P., Takegawa, N., Takemura, T., Textor, C., van Aardenne, J. A., and Zhao, Y.: Evaluation of black carbon estimations in global aerosol models, Atmos. Chem. Phys., 9, 9001–9026, doi:10.5194/acp-9-9001-2009, 2009.

Kok, J. F.: A scaling theory for the size distribution of emitted dust aerosols suggests climate models underestimate the size of the global dust cycle, P. Natl. Acad. Sci., 108, 1016–1021, 2011.

Kondo, Y., Oshima, N., Kajino, M., Mikami, R., Moteki, N., Takegawa, N., Verma, L. R., Kajii, Y., Kato, S., and Takami, A.: Emissions of black carbon in East Asia estimated from observations at a remote site in the East China Sea, J. Geophys. Res., 116, D16201, doi:10.1029/2011JD015637, 2011.

Kopacz, M., Jacob, J. D., Henze, K. D., Heald, L. C., Streets, G. D., and Zhang. Q.: A comparison of analytical and adjoint Bayesian inversion methods for constraining Asian sources of CO using satellite (MOPITT) measurements of CO columns, J. Geophys. Res., 114, D04305, doi:10.1029/2007JD009264, 2009.

Kopacz, M., Jacob, D. J., Fisher, J. A., Logan, J. A., Zhang, L., Megretskaia, I. A., Yantosca, R. M., Singh, K., Henze, D. K., Burrows, J. P., Buchwitz, M., Khlystova, I., McMillan, W. W., Gille, J. C., Edwards, D. P., Eldering, A., Thouret, V., and Nedelec, P.: Global estimates of CO sources with high resolution by adjoint inversion of multiple satellite datasets (MOPITT, AIRS, SCIAMACHY, TES), Atmos. Chem. Phys., 10, 855–876, doi:10.5194/acp-10-855-2010, 2010.

ACPD
14, 28385–28452, 2014

Kopacz, M., Mauzerall, D. L., Wang, J., Leibensperger, E. M., Henze, D. K., and Singh, K.: Origin and radiative forcing of black carbon transported to the Himalayas and Tibetan Plateau, Atmos. Chem. Phys., 11, 2837–2852, doi:10.5194/acp-11-2837-2011, 2011.

Krol, M., Houweling, S., Bregman, B., van den Broek, M., Segers, A., van Velthoven, P., Peters, W., Dentener, F., and Bergamaschi, P.: The two-way nested global chemistry-transport zoom model TM5: algorithm and applications, Atmos. Chem. Phys., 5, 417–432, doi:10.5194/acp-5-417-2005, 2005.

Ku, B. and Park, J. R.: Inverse modeling analysis of soil dust sources over East Asia, Atmos. Environ., 45, 5903–5912, doi:10.1016/j.atmosenv.2011.06.078, 2011.

Levelt, P. F., van den Oord, G. H. J., Dobber, M. R., Mälkki, A., Visser, H., de Vries, J., Stammes, P., Lundell, J. O. V., Saari, H.: The ozone monitoring instrument, IEEE T. Geosci. Remote, 44, 1093–1101, doi:10.1109/TGRS.2006.872333, 2006a.

Levelt, P. F., Hilsenrath, E., Leppelmeier, G. W., van den Oord, G. H. J., Bhartia, P. K., Tamminen, J., de Haan, J. F., Veefkind, J. P.: Science objectives of the ozone monitoring instrument, IEEE T. Geosci. Remote, 44, 1199–1208, doi:10.1109/TGRS.2006.872336, 2006b.

Li, Y., Henze, K. D., Jack, D., Henderson, B., and Kinney, P.: Assessing public health burden associated with exposure to ambient black carbon in the United States, Risk Analysis, in review, 2014.

Lions, J. L.: Optimal Control of Systems Governed by Partial Differential Equations, Springer-Verlag, Berlin, 1971.

Liu, H. Y., Jacob, J. D., Bey, I., and Yantosca, M. R.: Constraints from Pb-210 and Be-7 on wet deposition and transport in a global three-dimensional chemical tracer model driven by assimilated meteorological fields, J. Geophys. Res.-Atmos., 106, 12109–12128, 2001.

Liu, X. H., Penner, E. J., and Wang, M. H.: Influence of anthropogenic sulfate and black carbon on upper tropospheric clouds in the NCAR CAM3 model coupled to the IMPACT global aerosol model, J. Geophys. Res., 114, D03204, doi:10.1029/2008JD010492, 2009.

Lu, Z., Zhang, Q., and Streets, D. G.: Sulfur dioxide and primary carbonaceous aerosol emissions in China and India, 1996–2010, Atmos. Chem. Phys., 11, 9839–9864, doi:10.5194/acp-11-9839-2011, 2011.

Luo, M., Rinsland, C. P., Logan, J. A., Worden, J., Kulawik, S., Eldering, A., Goldman, A., Shephard, M. W., Gunson, M., and Lampel, M.: Comparison of carbon monoxide measurements by TES and MOPITT: The influence of a priori data and instrument characteristics on nadir

ACPD
14, 28385–28452, 2014

atmospheric species retrievals, J. Geophys. Res., 112, D09303, doi:10.1029/2006JD007663, 2007.
Magi, B. I., Ginoux, P., Ming, Y., and Ramaswamy, V.: Evaluation of tropical and extratropical Southern Hemisphere African aerosol properties simulated by a climate model, J. Geophys. Res.-Atmos., 114, D14204, doi:10.1029/2008JD011128, 2009.
Moorthy, K. K., Beegum, S. N., Srivastava, N., Satheesh, S. K., Chin, M., Blond, N., Babu, S. S., and Singh, S.: Performance evaluation of chemistry transport models over India, Atmos. Environ., 71, 210–225, 2013.
Omar, A. H., Winker, D. M., Tackett, J. L., Giles, D. M., Kar, J., Liu, Z., Vaughan, M. A., Powell, K. A., and Trepte, C. R.: CALIOP and AERONET aerosol optical depth comparisons: one size fits none, J. Geophys. Res.-Atmos., 118, 4748–4766, doi:10.1002/jgrd.50330, 2013.
Oshima, N., Koike, M., Zhang, Y., Kondo, Y., Moteki, N., Takegawa, N., and Miyazaki, Y.: Aging of black carbon in outflow from anthropo-genic sources using a mixing state resolved model: model development and evaluation, J. Geophys. Res., 114, D06210, doi:10.1029/2008JD010680, 2009.
Park, R. J., Jacob, J. D., Chin, M., and Martin, R. V.: Sources of carbonaceous aerosols over the United States and implications for natural visibility, J. Geophys. Res., 108, 4355, doi:10.1029/2002JD003190, 2003.
Philip, S., Martin, R. V., van Donkelaar, A., J., Lo, Wai-Ho, J., Wang, Y., Chen, D., Zhang, L., Kasibhatla, P. S., Wang, S. W., Zhang, Q., Lu, Z., Streets, G. D., Bittman, S., and Macdonald, J. D.: Global Chemical Composition of Ambient Fine Particulate Matter for Exposure Assessment, Environ. Sci. Technol., accepted, doi:10.1021/es502965b, 2014.
Punger, E. M. and West, J. J.: The effect of grid resolution on estimates of the burden of ozone and fine particulate matter on premature mortality in the USA, Air Qual. Atmos. Health, 6, 563–573, doi:10.1007/s11869-013-0197-8, 2013.
Qian, Y., Gustafson, W. I., Leung, L. R., and Ghan, S. J.: Effects of soot-induced snow albedo change on snowpack and hydrological cycle in western United States based on weather research and forecasting chemistry and regional climate simulations, J. Geophys. Res., 114, D03108, doi:10.1029/2008JD011039, 2009.
Ramanathan, V. and Carmichael, G.: Global and regional climate changes due to black carbon, Nat. Geosci., 1, 221–227, 2008.
Randerson, J. T., Liu, H., Flanner, M. G., Chambers, S. D., Jin, Y., Hess, P. G., Pfister, G., Mack, M. C., Treseder, K. K., Welp, L. R., Chapin, F. S., Harden, J. W., Goulden, M. L.,

ACPD
14, 28385–28452, 2014

Lyons, E., Neff, J. C., Schuur, E., Zender, C. S.: The impact of boreal forest fire on climate warming, Science, 314, 1130–1132, 2006.
Ridley, D. A., Heald, L. C., and Ford, B.: North African dust export and deposition: a satellite and model perspective, J. Geophys. Res., 117, D02202, doi:10.1029/2011JD016794, 2012.
Rodgers, C. D.: Inverse Methods for Atmospheric Sounding, Series on Atmospheric, Oceanic and Planetary Physics, vol. 2, World Scientific, Singapore, 2000.
Satheesh, S. K., Torres, O., Remer, L. A., Babu, S. S., Vinoj, V., Eck, T. F., Kleidman, R. G., and Holben, B. N.: Improved assessment of aerosol absorption using OMI-MODIS joint retrieval, J. Geophys. Res., 114, D05209, doi:10.1029/2008JD011024, 2009.
Schwartz, J., Coull, B., Laden, F., and Ryan, L.: The effect of dose and timing of dose on the association between airborne particles and survival, Environ. Health Persp., 116, 64–69, 2008.
Silva, A. R., West, J. J., Zhang, Y., Aneberg, C. S., Lamarque, J.-F., Shindell, T. D., Collins, J. W., Dalsoren, S., Faluvegl, G., Folbeth, G., Horowitz, W. L., Nagashima, T., Nalk, V., Rumbold, S., Skele, R., Sudo, K., Takemura, T., Bergmann, D., Camero-smith, P., Cionnl, I., Doherty, M. R., Eyring, V., Josse, B., MacKenzie, I. A., Plummer, D., Righl, M., Stevenson, S. D., Strode, S., Szopa, S., Zeng, G.: Global premature mortality due to anthropogenic outdoor air pollution and the contribution of past climate change, Environ. Res. Lett., 8, 034005, doi:10.1088/1748-9326/8/3/034005, 2013.
Sinyuk, A., Dubovik, O., Holben, B., Eck, T. F., Breon, F. M., Martonchik, J., Kahn, R., Diner, D. J., Vermote, E. F., Roger, J. C., Lapyonok, T., and Slutsker, I.: Simultaneous retrieval of aerosol and surface properties from a combination of AERONET and satellite data, Remote Sens. Environ., 107, 90–108, 2007.
Textor, C., Schulz, M., Guibert, S., Kinne, S., Balkanski, Y., Bauer, S., Berntsen, T., Berglen, T., Boucher, O., Chin, M., Dentener, F., Diehl, T., Feichter, J., Fillmore, D., Ginoux, P., Gong, S., Grini, A., Hendricks, J., Horowitz, L., Huang, P., Isaksen, I. S. A., Iversen, T., Kloster, S., Koch, D., Kirkevåg, A., Kristjansson, J. E., Krol, M., Lauer, A., Lamarque, J. F., Liu, X., Montanaro, V., Myhre, G., Penner, J. E., Pitari, G., Reddy, M. S., Seland, Ø., Stier, P., Takemura, T., and Tie, X.: The effect of harmonized emissions on aerosol properties in global models – an AeroCom experiment, Atmos. Chem. Phys., 7, 4489–4501, doi:10.5194/acp-7-4489-2007, 2007.

ACPD
14, 28385–28452, 2014

Torres, O., Bhartia, P. K., Herman, J. R., and Ahmad, Z.: Derivation of aerosol properties from satellite measurements of backscattered ultraviolet radiation, theoretical basis, J. Geophys. Res., 103, 17099–17110, doi:10.1029/98JD00900, 1998.

Torres, O., Bhartia, P. K., Sinyuk, A., Welton, E. J., and Holben, B.: Total Ozone Mapping Spectrometer measurements of aerosol absorption from space: comparison to SAFARI 2000 ground-based observations, J. Geophys. Res., 110, D10S18, doi:10.1029/2004JD004611, 2005.

Torres, O., Tanskanen, A., Veihelmann, B., Ahn, C., Braak, R., Bhartia, P. K., Veefkind, P., and Levelt, P.: Aerosols and surface UV products from ozone monitoring instrument observations: an overview, J. Geophys. Res., 112, D24S47, doi:10.1029/2007JD008809, 2007.

Torres, O., Ahn, C., and Chen, Z.: Improvements to the OMI near-UV aerosol algorithm using A-train CALIOP and AIRS observations, Atmos. Meas. Tech., 6, 3257–3270, doi:10.5194/amt-6-3257-2013, 2013.

United Nations Environment Program and World Meteorological Organization: Integrated Assessment of Black Carbon and Tropospheric Ozone, Nairobi, 2011.

van der Werf, G. R., Randerson, J. T., Giglio, L., Collatz, G. J., Kasibhatla, P. S., and Arellano Jr., A. F.: Interannual variability in global biomass burning emissions from 1997 to 2004, Atmos. Chem. Phys., 6, 3423–3441, doi:10.5194/acp-6-3423-2006, 2006.

van der Werf, G. R., Randerson, J. T., Giglio, L., Collatz, G. J., Mu, M., Kasibhatla, P. S., Morton, D. C., DeFries, R. S., Jin, Y., and van Leeuwen, T. T.: Global fire emissions and the contribution of deforestation, savanna, forest, agricultural, and peat fires (1997–2009), Atmos. Chem. Phys., 10, 11707–11735, doi:10.5194/acp-10-11707-2010, 2010.

Wang, J., Xu, X., Henze, K. D., Zeng, J., Ji, Q., Tsay, S.-C., and Huang, J.: Top-down estimate of dust emissions through integration of MODIS and MISR aerosol retrievals with the GEOS-Chem adjoint model, Geophys. Res. Lett., 39, L08802, doi:10.1029/2012GL051136, 2012.

Wang, Q., Jacob, D. J., Fisher, J. A., Mao, J., Leibensperger, E. M., Carouge, C. C., Le Sager, P., Kondo, Y., Jimenez, J. L., Cubison, M. J., and Doherty, S. J.: Sources of carbonaceous aerosols and deposited black carbon in the Arctic in winter-spring: implications for radiative forcing, Atmos. Chem. Phys., 11, 12453–12473, doi:10.5194/acp-11-12453-2011, 2011.

Wang, X., Wang, Y., Hao, J., Kondo, Y., Irwin, M., Munger, J. W., and Zhao, Y.: Top-down estimate of China's black carbon emissions using surface observations: sensitivity to observation representativeness and transport model error, J. Geophys. Res.-Atmos., 118, 5781–5795, doi:10.1002/jgrd.50397, 2013.

ACPD
14, 28385–28452, 2014

Wang, Y., Jacob, J. D., and Logan, A. J.: Global simulation of tropospheric O_3-NO_x-hydrocarbon chemistry, 1. Model formulation, J. Geophys. Res., 103, 10713–10726, 1998.
Wang, Y. X., McElroy, B. M., Jacob, J. D., and Yantosca, R. M.: A nested grid formulation for chemical transport over Asia: applications to CO, J. Geophys. Res., 109, D22307, doi:10.1029/2004JD005237, 2004.
Wecht, K. J., Jacob, D. J., Wofsy, S. C., Kort, E. A., Worden, J. R., Kulawik, S. S., Henze, D. K., Kopacz, M., and Payne, V. H.: Validation of TES methane with HIPPO aircraft observations: implications for inverse modeling of methane sources, Atmos. Chem. Phys., 12, 1823–1832, doi:10.5194/acp-12-1823-2012, 2012.
Wecht, K. J., Jacob, J. D., Frankenberg, C., Jiang, Z., and Blake, D. R.: Mapping of North American methane emissions with high spatial resolution by inversion of SCIAMACHY satellite data, J. Geophys. Res.-Atmos., 119, 7741–7756, doi:10.1002/2014JD021551, 2014.
Wesely, M. L.: Parameterization of surface resistance to gaseous dry deposition in regional-scale numerical models, Atmos. Environ., 23, 1293–1304, 1989.
Worden, H. M., Logan, J. A., Worden, J. R., Beer, R., Bowman, K., Clough, S. A., Eldering, A., Fisher, B. M., Gunson, M. R., Herman, R. L., Kulawik, S. S., Lampel, M. C., Luo, M., Meqretskaia, I. A., Osterman, G. B., and Shephard, M. W.: Comparisons of Tropospheric Emission Spectrometer (TES) ozone profiles to ozonesondes: methods and initial results, J. Geophys. Res., 112, D03309, doi:10.1029/2006JD007258, 2007.
Xu, X., Wang, J., Henze, K. D., Qu, W., Kopacz, M.: Constraints on aerosol sources using GEOS-Chem adjoint and MODIS radiances, and evaluation with multi-sensor (OMI, MISR) data, J. Geophys. Res., 118, 6396–6413, doi:10.1002/jgrd.50515, 2013.
Zhang, L., Jacob, J. D., Kopacz, M. Henze, K. D., Singh, K., and Jaffe, D. A.: Intercontinental source attribution of ozone pollution at western US sites using an adjoint method, Geophys. Res. Lett., 36, L11810, doi:10.1029/2009GL037950, 2009.
Zhang, L., Liao, H., Li, J.: Impacts of Asian summer monsoon on seasonal and interannual variations of aerosols over Eastern China, J. Geophys. Res., 115, D00K05, doi:10.1029/2009JD012299, 2010.
Zhang, L., Kok, J., Henze, K. D., Li, Q. B., and Zhao, C.: Improving simulations of fine dust surface concentrations over the Western United States by optimizing the particle size distribution, Geophys. Res. Lett., 40, 3270–3275, doi:10.1002/grl.50591, 2013.
Zhang, Q., Streets, D. G., Carmichael, G. R., He, K. B., Huo, H., Kannari, A., Klimont, Z., Park, I. S., Reddy, S., Fu, J. S., Chen, D., Duan, L., Lei, Y., Wang, L. T., and Yao, Z. L.: Asian

ACPD
14, 28385–28452, 2014

emissions in 2006 for the NASA INTEX-B mission, Atmos. Chem. Phys., 9, 5131–5153, doi:10.5194/acp-9-5131-2009, 2009.

Zhang, X. Y., Wang, Y. Q., Zhang, X. C., Guo, W., Gong, S. L., Zhao, P., and Jin, J. L.: Carbonaceous aerosol composition over various regions of China during 2006, J. Geophys. Res., 113, D14111, doi:10.1029/2007JD009525, 2008.

Zhao, C., Liu, X., Leung, L. R., Johnson, B., McFarlane, S. A., Gustafson Jr., W. I., Fast, J. D., and Easter, R.: The spatial distribution of mineral dust and its shortwave radiative forcing over North Africa: modeling sensitivities to dust emissions and aerosol size treatments, Atmos. Chem. Phys., 10, 8821–8838, doi:10.5194/acp-10-8821-2010, 2010.

Zhu, C., Byrd, R. H., Lu, P., and Nocedal, J.: L-BFGS-B: a Limited Memory FORTRAN Code for Solving Bound Constrained Optimization Problems, Tech. Rep., Northwestern University, 1994.

Zhu, L., Henze, K. D., Cady-Pereira, K. E., Shephard, M. W., Luo, M., Pinder, R. W., Bash, J. O., Jeong, G.: Constraining US ammonia emissions using TES remote sensing observations and the GEOS-Chem adjoint model, J. Geophys. Res., 118, 3355–3368, doi:10.1002/jgrd.50166, 2013.

ACPD
14, 28385–28452, 2014

Table 1. Comparison of BC anthropogenic emissions over eastern China (105–125° E, 20–45° N) and IGP (70–90° E, 23–32° N), unit: Tg.

Domain	Prior emissions (MEIC_SEAC4RS)		Posterior emissions (with penalty term)		Posterior emissions (without penalty term)	
	Apr	Oct	Apr	Oct	Apr	Oct
Eastern China	0.11	0.11	0.30	0.11	0.22	0.12
IGP	0.04	0.04	0.14	0.04	0.11	0.05

ACPD
14, 28385–28452, 2014

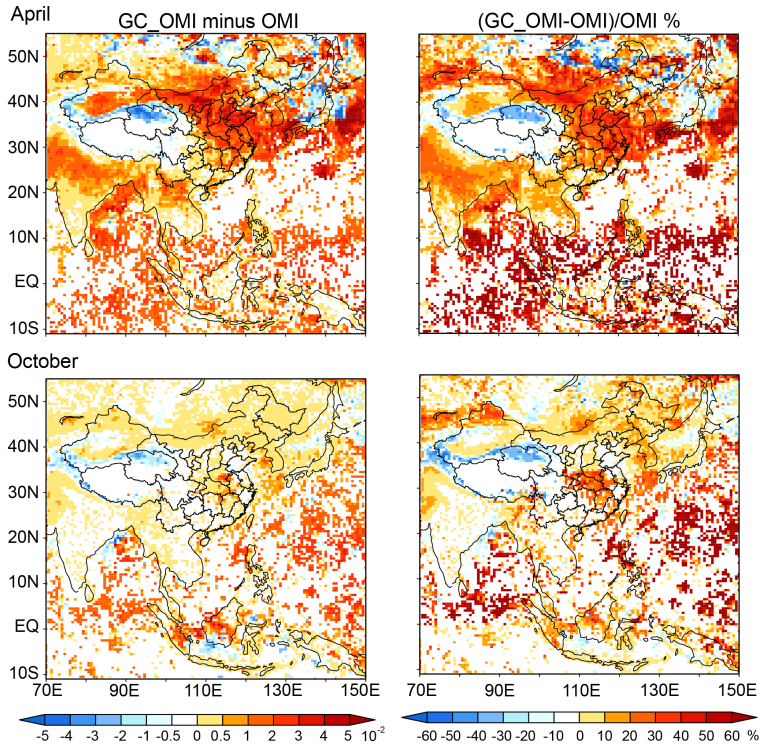

Figure 1. Absolute and relative differences in AAOD between OMI_Final and OMI_GC AAOD over Southeast Asia for April and October 2006.

ACPD
14, 28385–28452, 2014

Constraining black carbon using OMI AAOD and GEOS-Chem adjoint

L. Zhang et al.

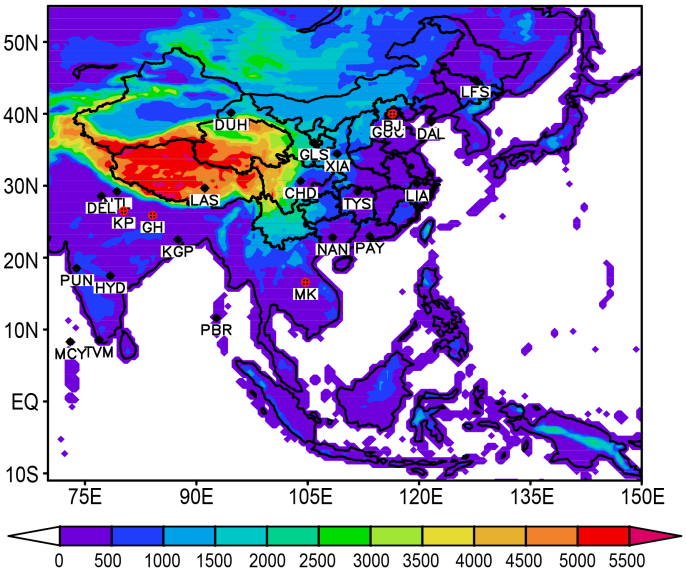

Figure 2. Twenty sites of ground measurements (black dots) and four sites of AERONET observation (red cross dots) over Southeast Asia. Also shown are terrain heights (color shaded contours, unit: m).

ACPD
14, 28385–28452, 2014

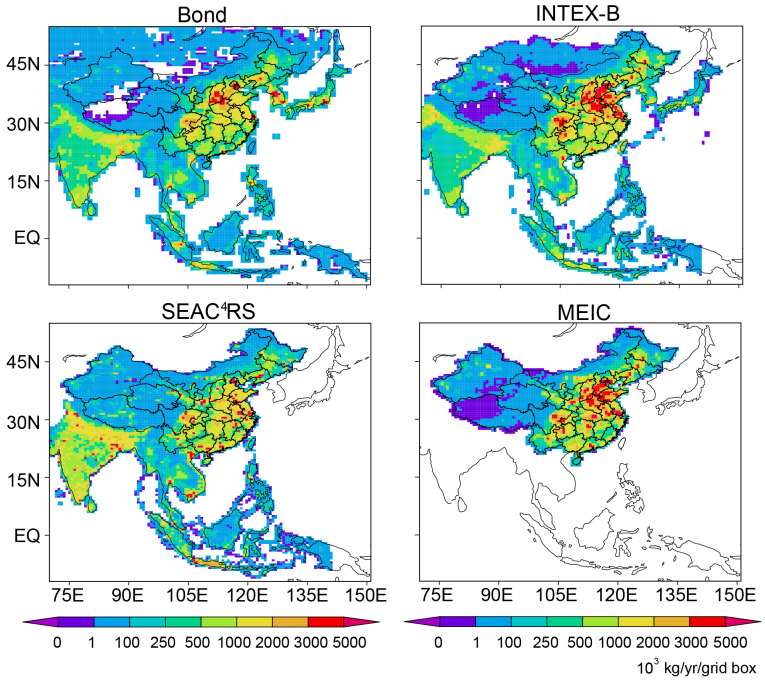

Figure 3. Annual anthropogenic emission of BC regridded into GEOS-Chem resolution of 0.5° × 0.667° from the inventories of Bond, INTEX-B, SEAC4RS, and MEIC.

ACPD
14, 28385–28452, 2014

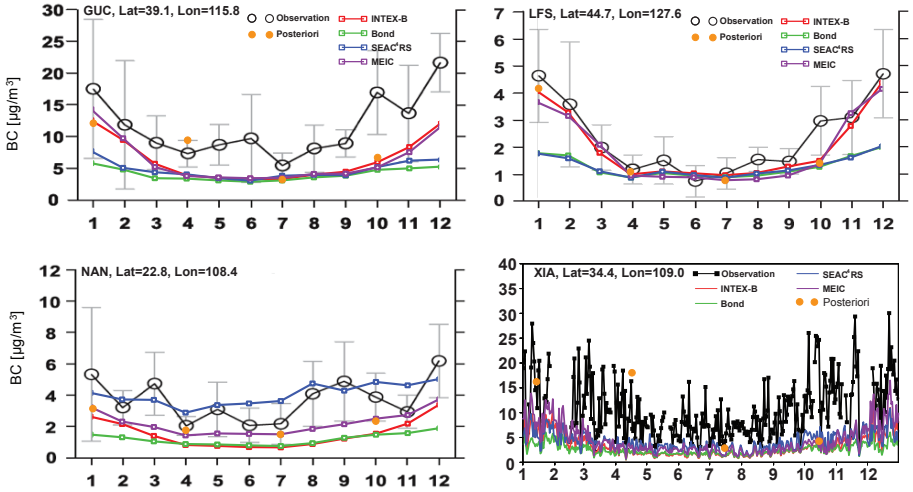

Figure 4. Comparison of the observed and simulated surface BC concentrations using four emission inventories at the site of GUC, LFS, NAN, XIA. The orange dots are the monthly mean posterior surface BC concentrations at these sites using MEIC inventory over China.

ACPD
14, 28385–28452, 2014

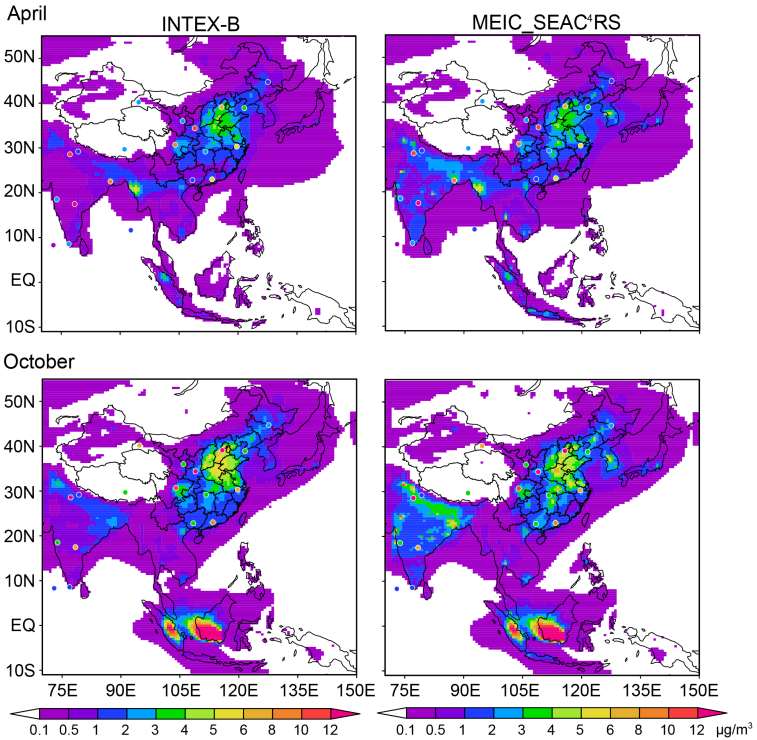

Figure 5. Spatial distributions of prior surface BC concentrations using INTEX-B and MEIC_SEAC4RS inventories overlaid with BC in situ measurements of 20 sites over Southeast Asia.

ACPD
14, 28385–28452, 2014

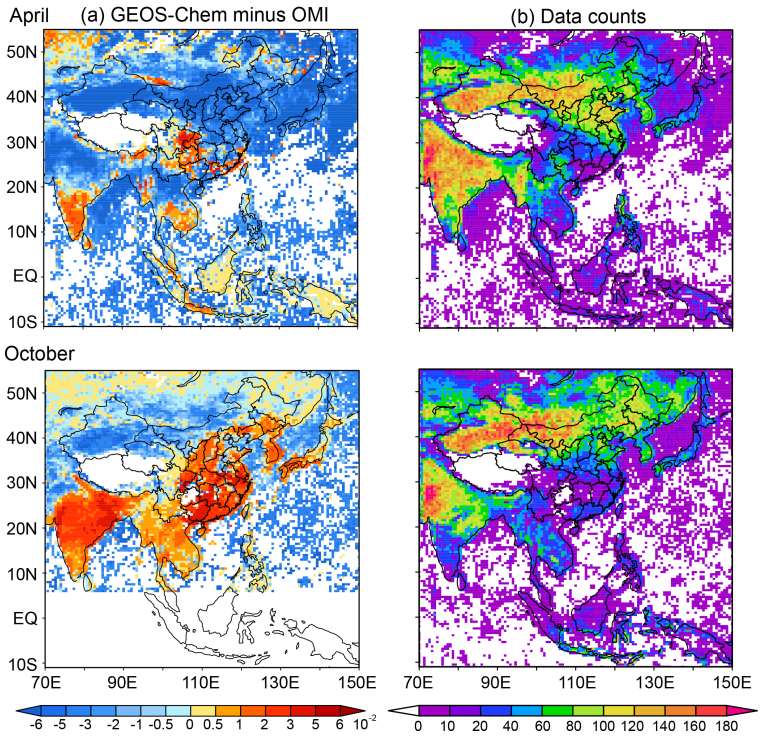

Figure 6. (a) Differences of monthly average AAOD between model using MEIC_SEAC4RS inventory and the OMI observation (former minus latter) and **(b)** corresponding OMI monthly data in each grid cell for April and October 2006.

ACPD
14, 28385–28452, 2014

Constraining black carbon using OMI AAOD and GEOS-Chem adjoint

L. Zhang et al.

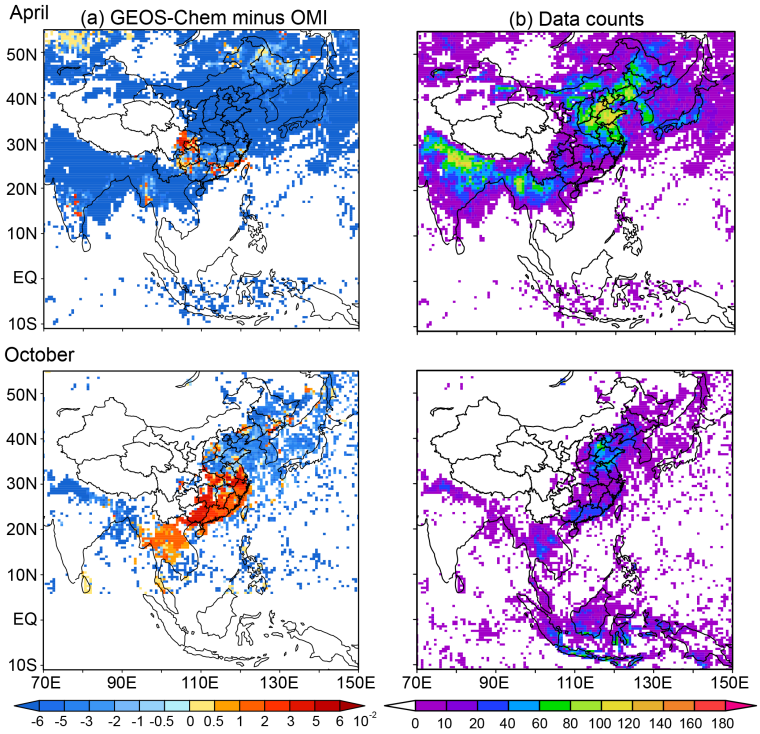

Figure 7. The same as Fig. 6, but for OMI_AAOD_BC.

ACPD
14, 28385–28452, 2014

Constraining black carbon using OMI AAOD and GEOS-Chem adjoint

L. Zhang et al.

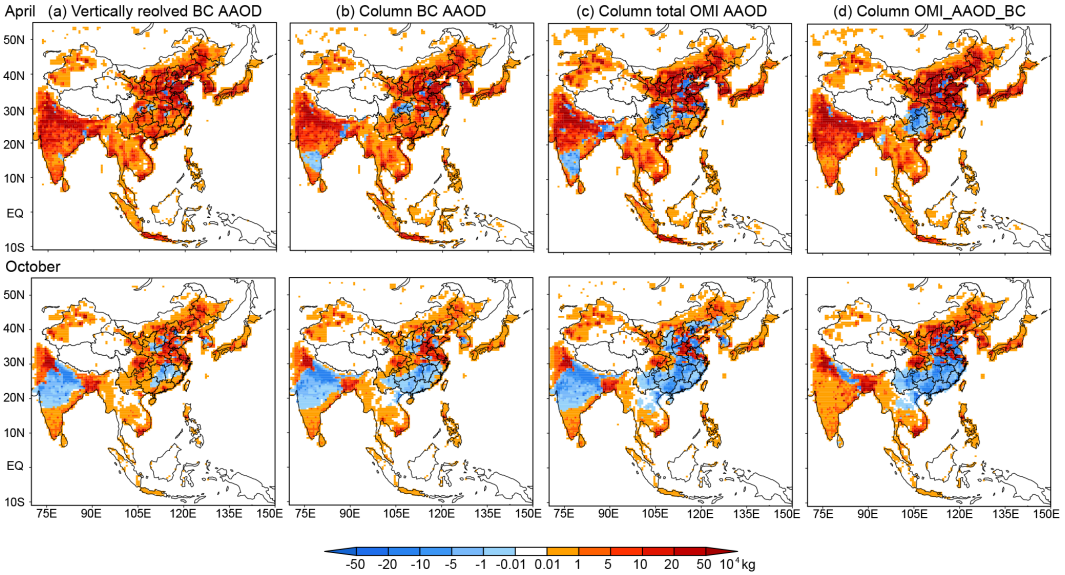

Figure 8. Differences between optimized and prior anthropogenic BC emissions based on four methods of adjoint forcing **(a)** vertically resolved BC AAOD base on model, **(b)** column BC AAOD based on model, **(c)** total OMI AAOD and **(d)** column OMI_AAOD_BC for April and October 2006.

ACPD
14, 28385–28452, 2014

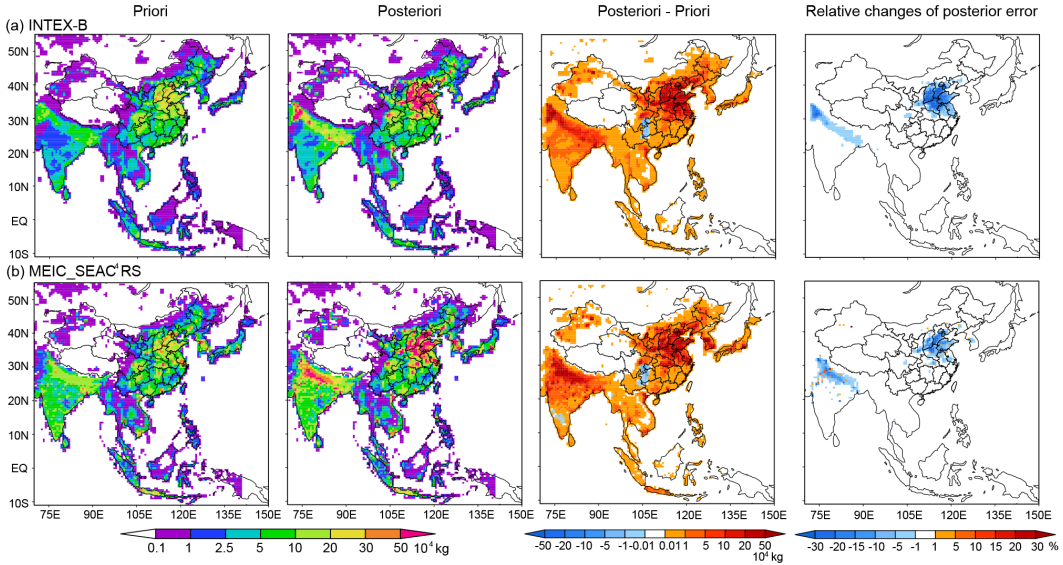

Figure 9. Anthropogenic BC emissions for April 2006. The first column shows the prior inventory, the second the optimized inventory, the third the differences between the prior and optimization, and the last column the relative changes of posterior error, based on the inventories of **(a)** INTEX-B and **(b)** MEIC_SEAC^{4}RS.

ACPD
14, 28385–28452, 2014

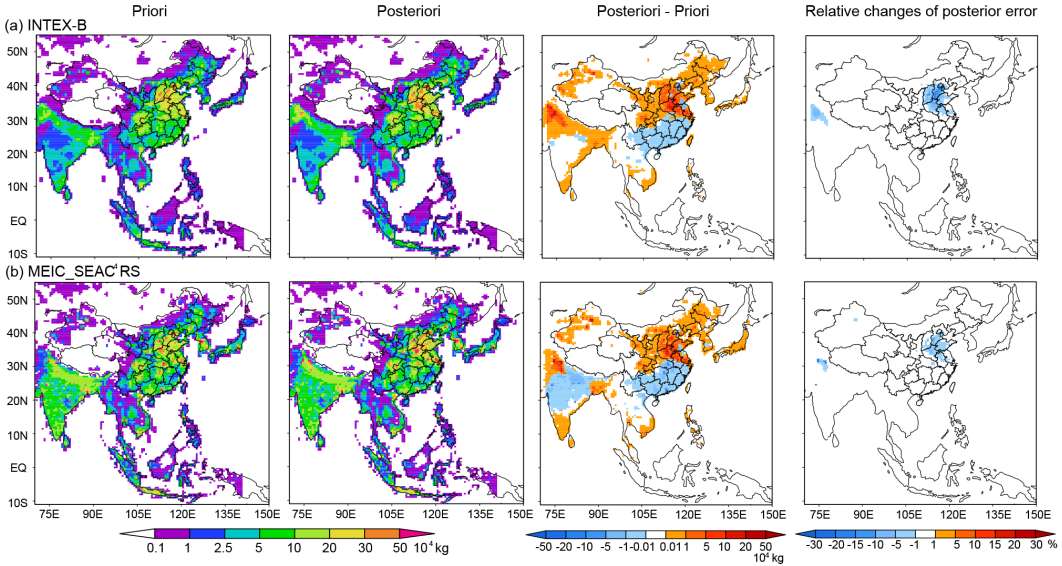

Figure 10. The same as Fig. 8, but for October 2006.

ACPD
14, 28385–28452, 2014

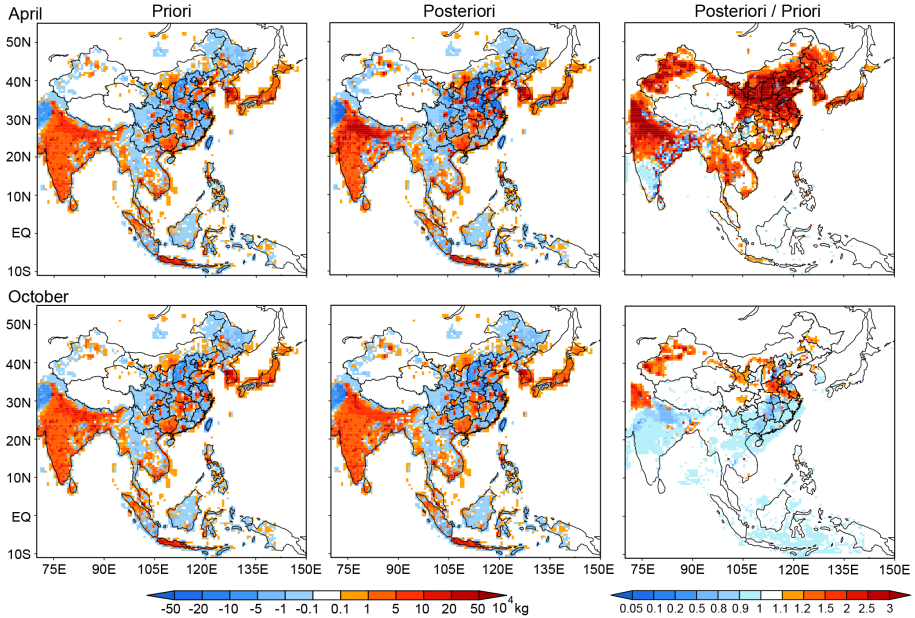

Figure 11. Differences of anthropogenic BC emissions between using the inventories of MEIC_SEAC4RS and INTEX-B for April and October 2006. The left column shows the prior inventory, the center the optimized inventory, and right column the between their posterior differences and prior differences.

ACPD
14, 28385–28452, 2014

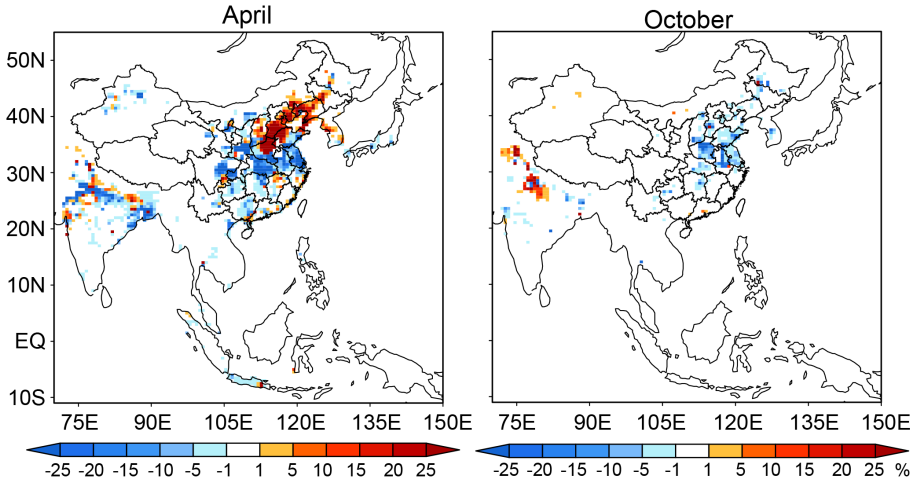

Figure 12. The sensitivities of optimized anthropogenic emission based on GFED2 and GFED3 relative to the differences between GFED2 and GFED3.

ACPD
14, 28385–28452, 2014

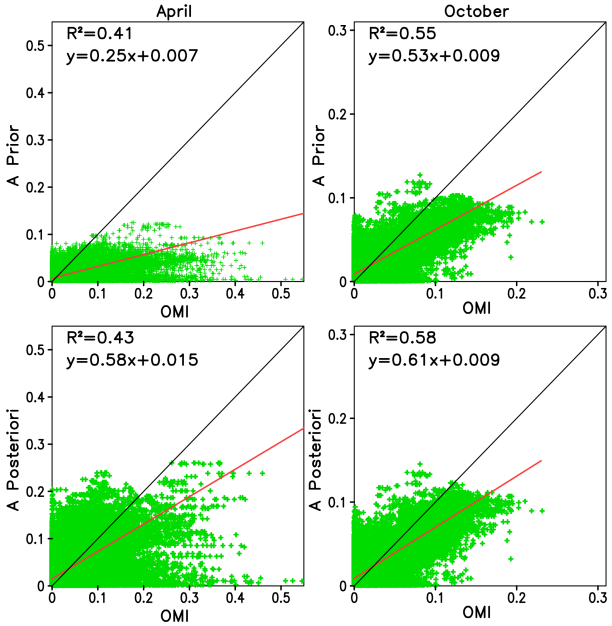

Figure 13. Comparison of BC AAOD over eastern China (105–125° E, 20–45° N) from OMI measurements and GEOS-Chem before and after the assimilation for April and October 2006.

ACPD
14, 28385–28452, 2014

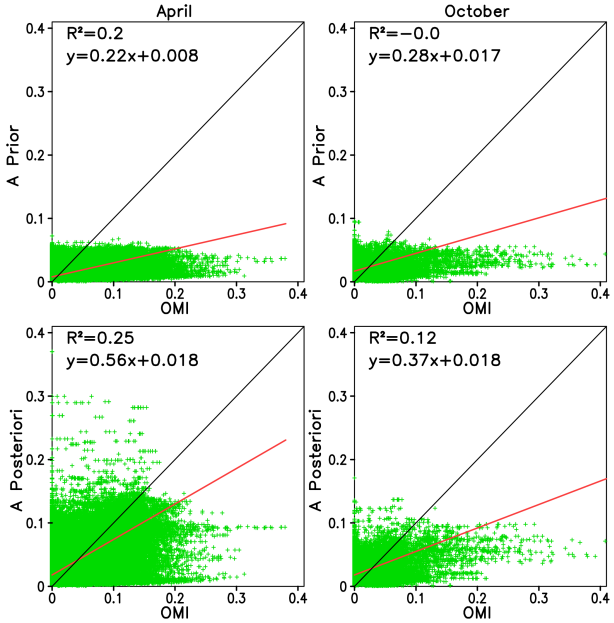

Figure 14. Comparison of BC AAOD over IGP (70–90° E, 23–32° N) from OMI measurements and GEOS-Chem before and after the assimilation for April and October 2006.

ACPD
14, 28385–28452, 2014

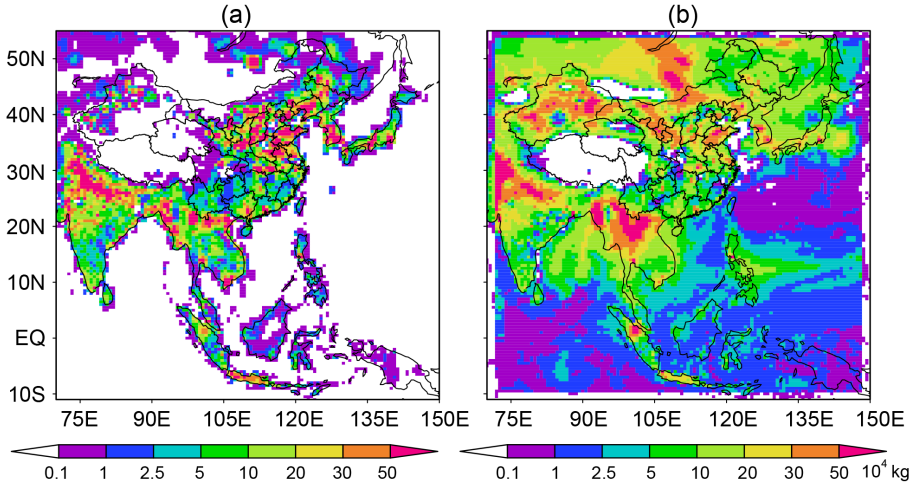

Figure 15. Optimized total emissions using inversion approaches of **(a)** scaling factor based and **(b)** emission based.

ACPD
14, 28385–28452, 2014

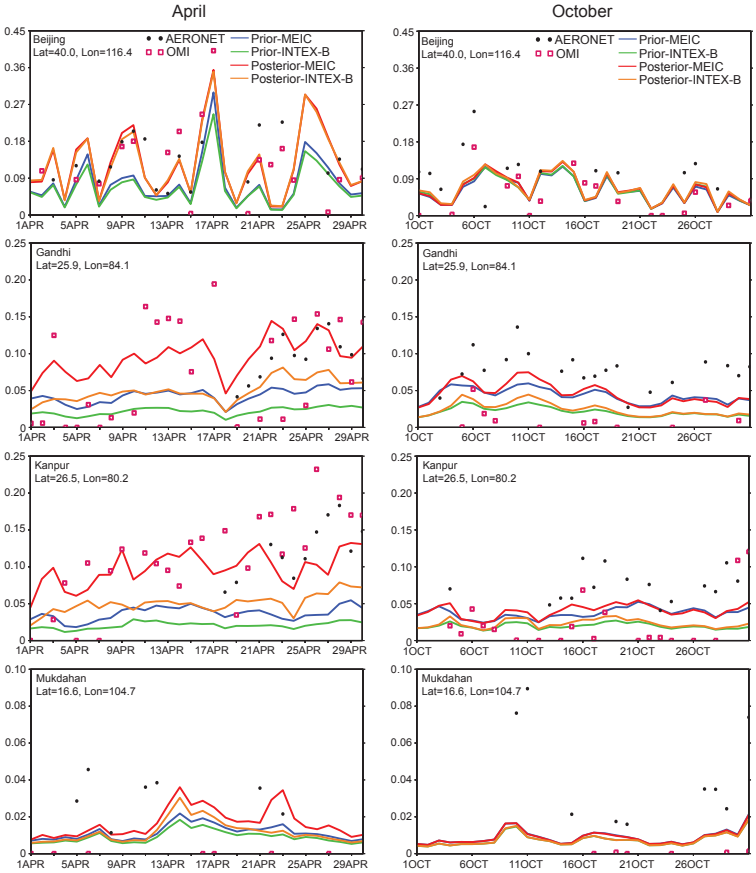

Figure 16. Comparison of total daily AAOD from OMI, AERONET and GEOS-Chem before and after the assimilation at the four AERONET sites for April and October 2006.

ACPD
14, 28385–28452, 2014

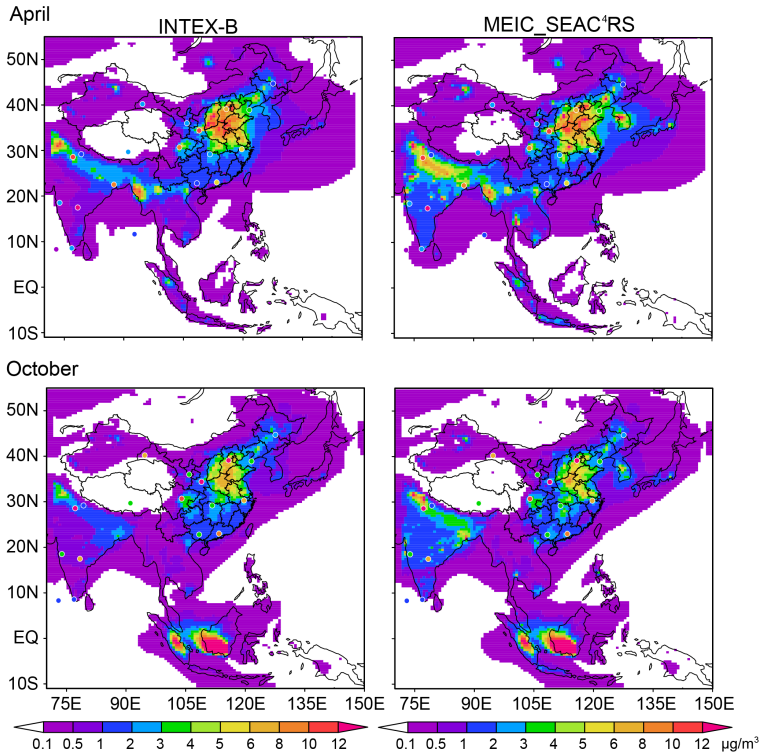

Figure 17. Spatial distributions of optimized surface BC concentrations using INTEX-B and MEIC_SEAC4RS inventories overlaid with BC in situ measurements of 20 sites over Southeast Asia.

ACPD
14, 28385–28452, 2014

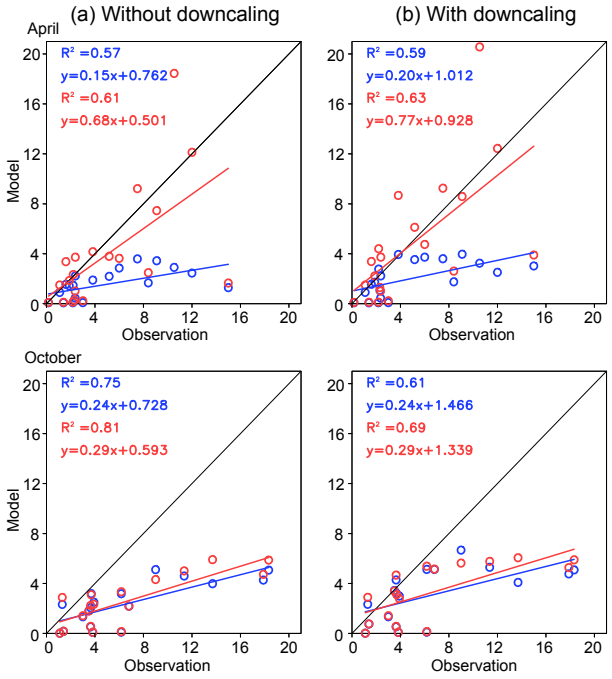

Figure 18. Comparison of monthly surface BC concentration over Southeast Asia for April and October 2006, from in situ measurements and GEOS-Chem before and after the assimilation **(a)** without and **(b)** with population density downscaling.

ACPD
14, 28385–28452, 2014

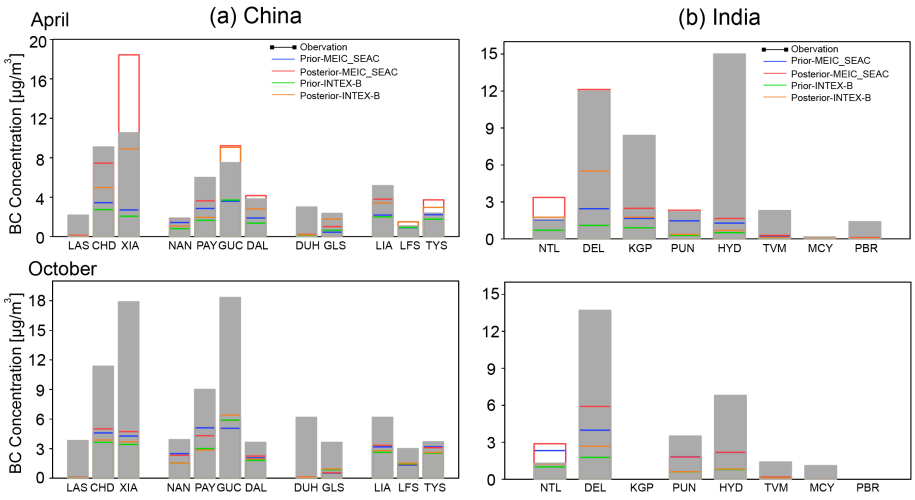

Figure 19. Comparison of monthly surface BC concentration from in situ measurements and GEOS-Chem over **(a)** China and **(b)** Indan before and after the assimilation using the inventories of MEIC_SEAC4RS and INTEX-B for April and October 2006.

ACPD
14, 28385–28452, 2014

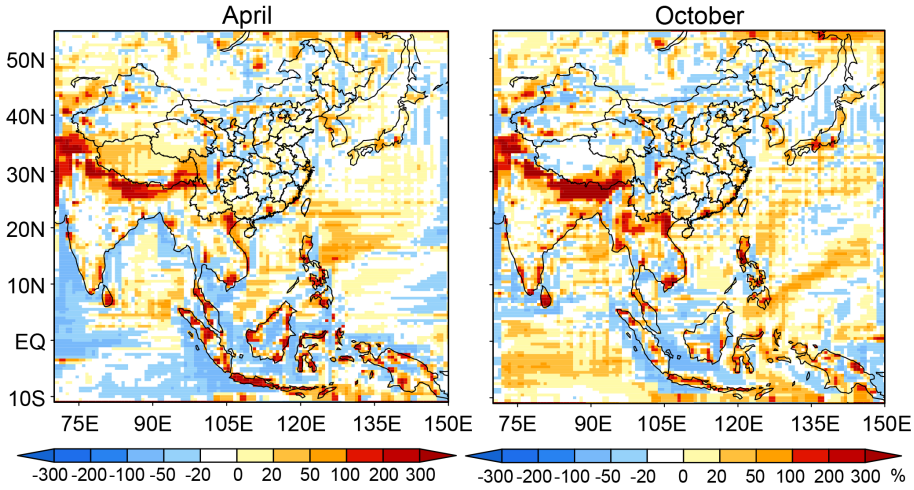

Figure 20. The resolution errors of surface BC between the simulations of coarse resolution ($2^{\circ} \times 2.5^{\circ}$) and fine resolution ($0.5^{\circ} \times 0.667^{\circ}$).

ACPD
14, 28385–28452, 2014

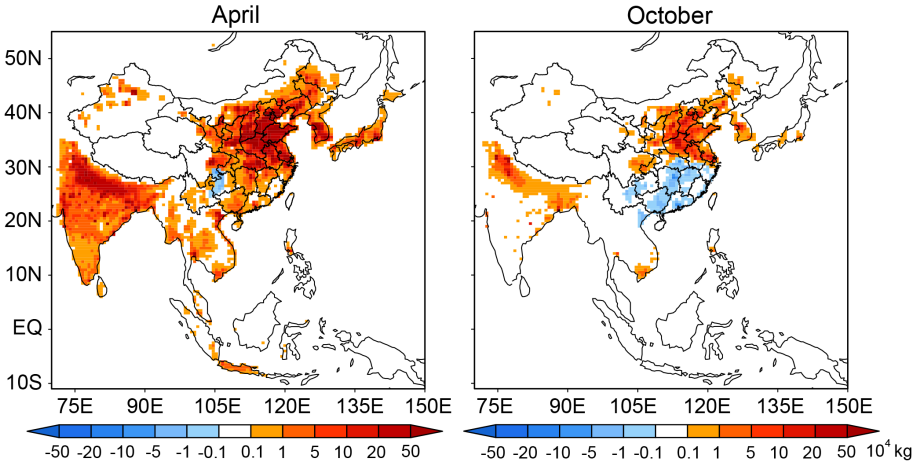

Figure 21. The differences between the prior and posterior anthropogenic BC emissions for April and October 2006, using OMI_AAOD_BC as the observation.

ACPD
14, 28385–28452, 2014